Optical Behavior of III-TM-N Materials And Devices

Contract No. ARO-W911-NF-04-1-0296

Contract Monitor: Dr. J. Zavada

FINAL REPORT

T.O.C. : **C. R. Abernathy**
Dept. of Materials Sci. and Eng.
University of Florida
Gainesville, FL 32606

Report Documentation Page

Form Approved
OMB No. 0704-0188

1. REPORT DATE	2. REPORT TYPE	3. DATES COVERED
26 SEP 2008		**01-10-2004 to 31-12-2007**

4. TITLE AND SUBTITLE	5a. CONTRACT NUMBER
Optical Behavior of III-TM-N Materials And Devices	5b. GRANT NUMBER
	5c. PROGRAM ELEMENT NUMBER
6. AUTHOR(S)	5d. PROJECT NUMBER
	5e. TASK NUMBER
	5f. WORK UNIT NUMBER
7. PERFORMING ORGANIZATION NAME(S) AND ADDRESS(ES) **University of Florida,Dept. of Materials Sci. and Eng., Sponsored Research Office,29 Grinter Hall,Gainesville,FL,32611**	8. PERFORMING ORGANIZATION REPORT NUMBER
9. SPONSORING/MONITORING AGENCY NAME(S) AND ADDRESS(ES)	10. SPONSOR/MONITOR'S ACRONYM(S)
	11. SPONSOR/MONITOR'S REPORT NUMBER(S)

12. DISTRIBUTION/AVAILABILITY STATEMENT
Approved for public release; distribution unlimited

13. SUPPLEMENTARY NOTES

14. ABSTRACT

15. SUBJECT TERMS

16. SECURITY CLASSIFICATION OF:			17. LIMITATION OF ABSTRACT	18. NUMBER OF PAGES	19a. NAME OF RESPONSIBLE PERSON
a. REPORT	b. ABSTRACT	c. THIS PAGE			
unclassified	**unclassified**	**unclassified**	**Same as Report (SAR)**	**44**	

SUMMARY

Room temperature ferromagnetism has been observed in AlMnN grown by gas-source MBE. The lattice constant decreased with increasing Mn cell temperature for single phase material, indicating constant site occupation, probably substitutional. Hysteresis in M vs. H at room temperature was observed in single phase material and the magnetization as a function of temperature suggests ferromagnetism caused by AlMnN, not clusters. AlCrN was also investigated. Strong ferromagnetism persists to 350K (the temperature limit of the SQUID magnetometer), in the optimized AlCrN. Moreover, the saturation magnetization remains unchanged in the temperature region from 10K-350K. By contrast, AlMnN films grown under similar conditions were found to decrease in magnetization at 300K as compared to 100K. This suggests that AlCrN has a Curie point above that of AlMnN. Moreover, the Curie temperature of AlCrN is well above room temperature whereas the Curie temperature of AlMnN is in the vicinity of room temperature. Overall, Cr tends to be a better dopant than Mn in ferromagnetic AlN.

The thermal stability of optimal epi-AlCrN was investigated and was found to be poorer than that of GaCrN. The upper limit of anneal temperature before destruction of magnetic properties was found to be 700°C. No indication of second phases was observed after the 700°C anneal, which implies that the RTA was not significant enough to destroy the single phase AlCrN. However, although the single phase AlCrN withstood the RTA, the magnetic interaction within the material did not. This suggests that the mechanism for magnetization within this particular DMS is too weak to endure routine processing procedures during fabrication, such as the annealing of ohmic contacts. Hence, processing procedures must be altered for incorporation into current technology or alternate materials will need to be used in place of AlCrN.

Growth of GaGdN was also explored. The incorporation of Gd into GaN results in an overall improvement of magnetic properties. The magnetization is increased relative to GaCrN and GaMnN, although the dopant concentration is lower. GaGdN films were ferromagnetic above room temperature, with magnetization that does not appear to be due to interfacial effects. The amount of Gd incorporated into the films is extremely low and results in highly resistive films. The ferromagnetic behavior of this material follows models of long range spin polarization. In addition, co-doping with Si shows larger overall magnetic signal and results in a conductive, n-type material.

The thermal stability of the optimal GaGdN (T_{Gd} = 1050°C) was investigated. The material was annealed from 300°C to 700°C to determine the temperature at which magnetization is destroyed. M vs. H measurements taken at 300K for each anneal temperature indicate the change in magnetization with anneal temperature. After annealing, the saturation magnetization decreases by a factor of greater than one half. Although the maximum magnetic signal decreases, the overall hysteresis increases. The loop becomes more square, with an increase in magnetic remanence and coercivity. One possible explanation of the hardening involves a change in domain structure. The high anneal temperature may alter the domain structure in such a way as to make the domains less easy to manipulate, thereby requiring a stronger magnetic field to produce zero magnetization. The increase in remanence with anneal temperature indicates the retention of more magnetic alignment within the material. Therefore, it seems plausible that annealing the GaGdN creates an alteration within the domain structure producing a larger coercivity and remanence. Also, the decrease in saturation magnetization indicates a decrease in the strength of the magnetic interactions within the GaGdN.

GaN films were doped with Eu to a concentration of ~0.12 at. % during growth at 800 °C by molecular beam epitaxy, with the Eu cell temperature held constant at 470°C. All samples were post-growth annealed at 675 °C. The films exhibited strong photoluminescence (PL) in the red (622 nm) whose absolute intensity was a function of the Ga flux during growth, which ranged from $3.0x10^{-7}$ to $5.4x10^{-7}$ Torr. The maximum PL intensity was obtained at a Ga flux of $3.6x10^{-7}$ Torr. The samples showed room temperature ferromagnetism with saturation magnetization of ~0.1–0.45 emu/cm^3, consistent with past reports where the Eu was found to be predominantly occupying substitutional Ga sites. There was an inverse correlation between the PL intensity and the saturation magnetization in the films. X-ray diffraction showed the presence of EuGa phases under all the growth conditions but these cannot account for the observed magnetic properties.

2.0 Results and Discussion

2.1 ALN-BASED DILUTE MAGNETIC SEMICONDUCTOR GROWTH AND CHARACTERIZATION

Growth of the films presented occurred in a Varian Gen II by gas-source molecular beam epitaxy. Solid Al(7N) and Mn(7N) sources were heated in standard effusion cells. Gaseous nitrogen was supplied by an Oxford rf plasma head. All films were grown on (0001) oriented sapphire substrates, indium mounted to Mo blocks. AlMnN and AlN films were grown at a temperature of 780°C, as indicated by the substrate heater thermocouple. A nitrogen flow of 1.3 standard cubic centimeters per minute (sccm) corresponded to a chamber pressure of $2.3x10^{-5}$ Torr during the growth of the films. Sapphire substrates were first nitridated for 30 minutes at a substrate temperature of 1000°C under 1.1 sccm nitrogen (chamber pressure = $1.9x10^{-5}$ Torr). Nucleation at 575°C for 10 minutes and a 30 minute buffer layer at 950° C followed nitridation, both under 1.1 sccm nitrogen. Both AlN and AlMnN films were grown with a substrate temperature of 780°C and an Al effusion cell temperature of 1150°C. The Mn cell temperature (T_{Mn}) was varied from 635°C to 658°C. The growth rate of the AlN was 0.2μm/hr and the growth rate of the AlMnN films was 0.16μm/hr.

In situ reflection high energy electron diffraction (RHEED) was used to monitor films during growth. AlN demonstrated 2D growth and AlMnN films demonstrated 2D/3D growth. Determination of the phase composition of the layers was carried out by x-ray diffraction in a Phillips APD powder diffractometer. AlMnN grown with a Mn cell temperature of 635°C was found to be single phase. The AlMnN with T_{Mn}=658°C formed AlMn as detected by powder x-ray diffraction (XRD). A Mn cell temperature of 650°C was found to be the upper limit of single phase AlMnN under previously mentioned growth conditions. For comparison, a layer of Mn_4N was also grown on sapphire. Auger Electron Spectroscopy (AES) showed Mn to be present in all of the Mn films, however accurate determination of the Mn concentration in AlMnN was hindered by the small Mn signals. It is estimated that AlMnN films contain no more than 1% Mn.

Crystalline quality of the films was inspected using high resolution x-ray diffraction (HRXRD) in a Philips X'pert diffractometer equipped with a Cu K_α source. Rocking curves were performed on films in order to determine the FWHM and lattice constants of the films. Lattice constants were calculated using Bragg's law from data obtained by the HRXRD investigation. Table 1 shows results of those calculations for AlN and AlMnN grown using two different Mn cell temperatures. The lattice constant was found to decrease as the Mn cell temperature increased for single phase material. A similar pattern was observed for single phase GaMnN films grown in the same system under different conditions. GaN implanted with Mn has been reported to exhibit substitutional or near substitutional incorporation. It is expected that the incorporation of interstitial Mn should either increase or have no effect on the lattice constant. The observation of a decrease in the lattice constant of the AlMnN films suggests that the Mn occupies a substitutional site. This is further confirmed by Hall analysis, also given in Table I, which shows pure AlN to be highly resistive as expected and material containing an AlMn second phase to be highly conductive n-type. By contrast, single phase AlMnN was found to be p-type. If Mn incorporates substitutionally, one would expect by analogy with its behavior in

other III-V materials that it would behave as a deep acceptor. The observation of p-type behavior fits this explanation.

Table 1. Table featuring the lattice constant and electrical properties of AlMnN and AlCrN films.

	Lattice Constant (Ang)	FWHM	Carrier Type/ Concentration (cm^{-3})	Resistivity (Ωcm)
AlN	4.89592	0.0919	-	insulating
AlMnN (TMN=635°C)	4.89292	0.0928	-	-
AlMnN (TMN=650°C)	4.89169	0.0902	p-type/~1E18	1.6
AlMnN/AlMn	4.89326	0.0984	n-type/~2E20	5.7E-3
AlCrN			-	-
AlCrN/Al_xCr_y +Cr_2N				1000

Magnetic measurements were performed on samples using a Quantum Design MPMS SQUID magnetometer. Magnetization as a function of magnetic field and temperature was measured with the applied field parallel to all films. Magnetic remanence and coercivity indicating hysteresis was observed in ternary AlMnN films at 10, 100, and 300K. As a rough estimate, saturation magnetization was extracted from the hysteresis loops as the magnetization at 1000 Gauss (G). This estimated saturation magnetization was found to decrease at 300K compared to 100K for AlMnN grown at T_{Mn}=650°C. Also, the remanent magnetization was extracted from the hysteresis loops and was found to decrease with temperature. The values of temperature dependent estimated saturation magnetization and remanent magnetization of AlMnN are shown in Figure 1. A comparison of the M vs. H loops at 10K and 300K of the AlMnN shows a large decrease in observed hysteresis, as shown in Figure 2. This decrease in the overall magnetization as seen in the M vs. H loops possibly indicates that the Curie temperature of the AlMnN is just beyond 300K. However, clear hysteresis is evident at room temperature. The coercive field (approximately 70 Gauss) was found to be independent of temperature. Undoped AlN grown under the same conditions as AlMnN demonstrated paramagnetic behavior, as shown in Figure 3. This indicates that hysteresis arises with the addition of Mn. The diamagnetic background due to the sapphire substrate was subtracted from the raw data and the subsequent corrected data was used for analysis. The magnetization was not normalized to the Mn concentration due to the inability of AES to precisely detect the small amount of Mn in the films.

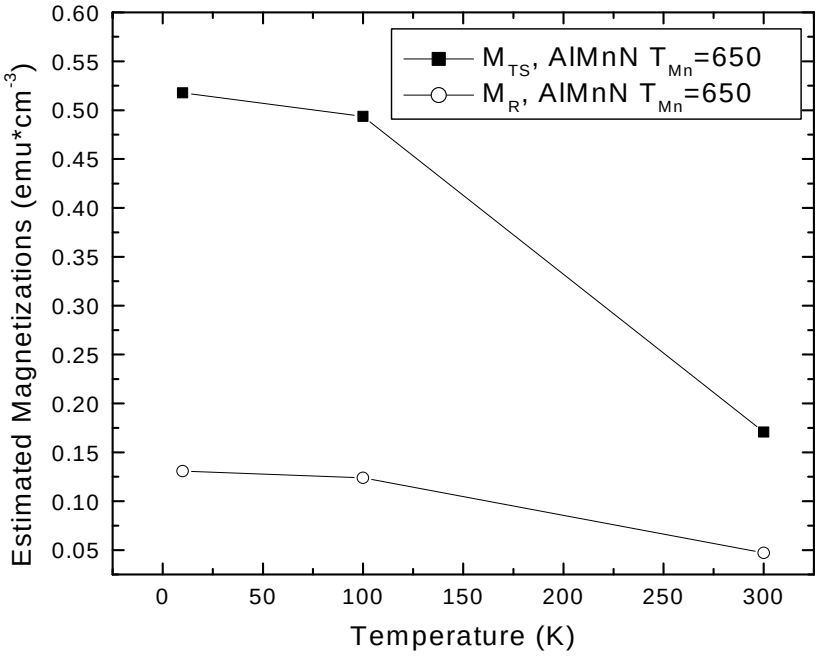

Figure 1. Estimated saturation magnetization and estimated remanent magnetization of AlMnN. The film was grown with Mn cell temperature of 650°C and under a nitrogen flow of 1.3 sccm.

Clusters of second phases, undetectable by methods mentioned above, are not thought to be the cause of hysteresis observed at 300K. This is supported by magnetic analysis of material containing the most likely cluster phases, AlMn and Mn_4N. Magnetization as a function of temperature for AlN, single phase AlMnN, AlMnN with an AlMn phase present, and Mn_4N show substantially different behavior, as shown in Fig. 4. The reason for the low T(10-50K) behavior seen in AlN and AlMnN films is still unknown. The M vs. T of Mn_4N clearly indicates ferromagnetic behavior, and the formation of clusters has been proposed as the cause of hysteresis in some ferromagnetic III-V materials. However, the formation of Mn_4N clusters does not influence the magnetization above 50K, since clearly the magnetization drops to zero at that temperature. Also, the magnetization vs. temperature indicates that the formation of AlMn clusters is not the cause of the ferromagnetism observed, evidenced by the order of magnitude difference between the values of magnetization over 150K. Hence, the incorporation of Mn into the AlN lattice forming the ternary AlMnN is most likely the reason for the observed hysteresis.

In conclusion, room temperature ferromagnetism has been observed in AlMnN grown by gas-source MBE. The lattice constant decreased with increasing Mn cell temperature for single phase material, indicating constant site occupation, probably substitutional. Hysteresis in M vs. H at room temperature was observed in single phase material and the magnetization as a function of temperature suggests ferromagnetism caused by AlMnN, not clusters.

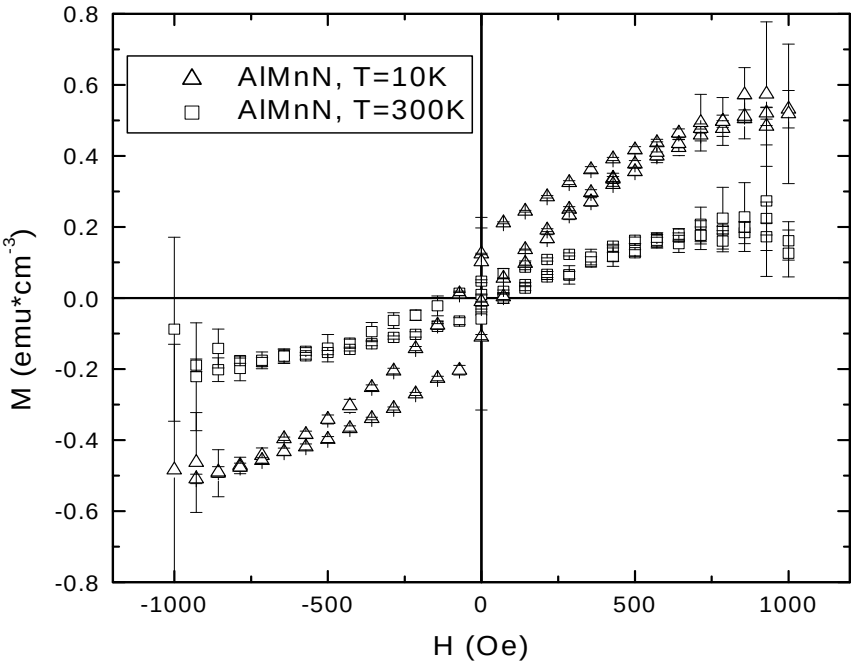

Figure 2. Magnetization versus applied magnetic field for AlMnN at temperatures of 10K and 300K. The film was grown with a Mn cell temperature of 650°C and under a nitrogen flow of 1.3 sccm.

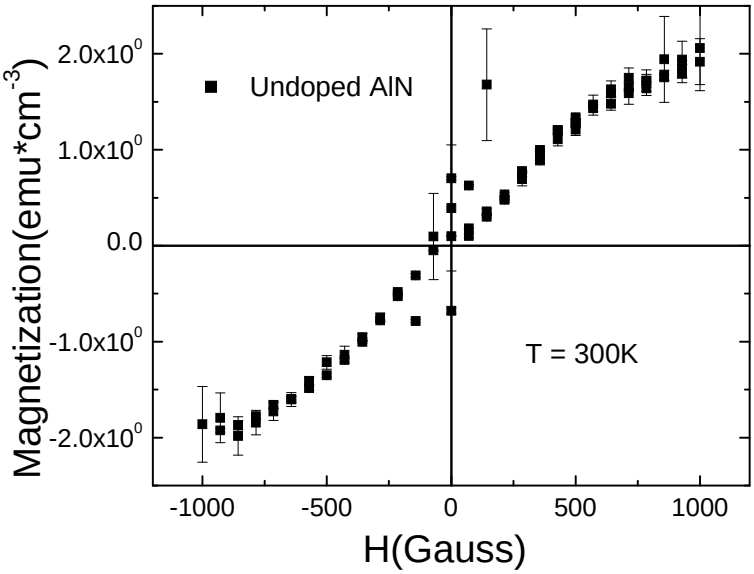

Figure 3. Magnetization vs. applied field of the undoped AlN showing paramagnetic behavior.

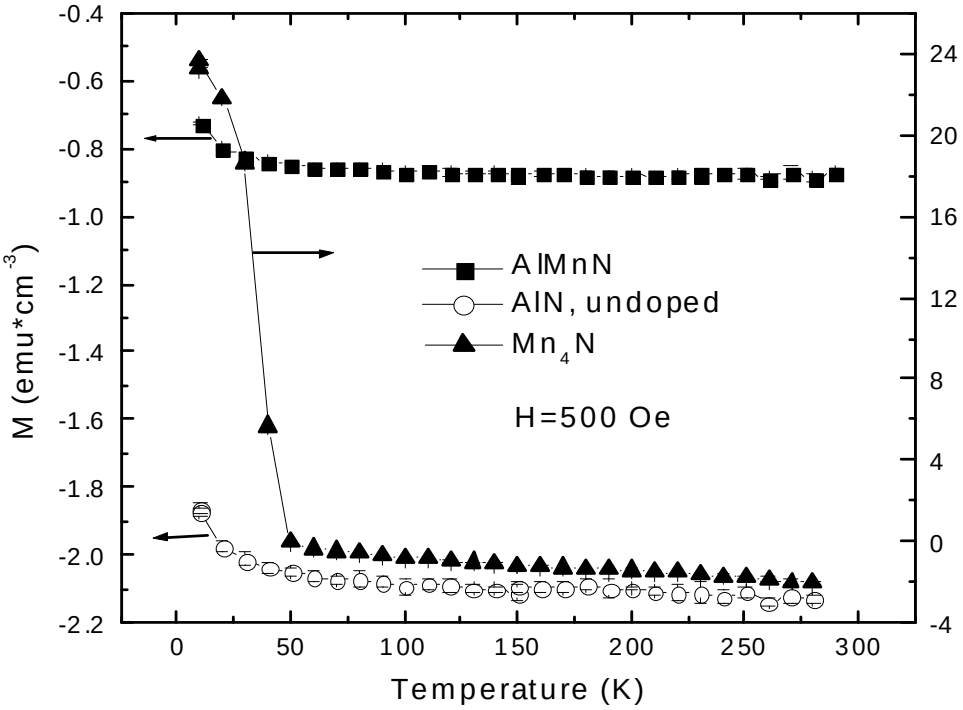

Figure 4. Magnetization versus temperature for films of either undoped AlN, single phase AlMnN, or Mn_4N.

AlCrN films were grown by Molecular Beam Epitaxy (MBE) on c-plane sapphire in a similar fashion to the AlMnN films discussed in the previous section. The same Al and nitrogen sources were used, and the same nitridation, nucleation, and high temperature buffer layers were grown prior to DMS growth. Solid Cr (7N) was used as the dopant source in the AlCrN films by heating in a standard effusion cell. AlCrN films were grown at a substrate thermocouple temperature reading (T_S) of 780°C. The AlCrN films were grown with a Cr cell temperature thermocouple reading (T_{Cr}) from 982-1005°C. The Cr concentrations were in the range 1-3 at. %, as measured by x-ray microprobe and secondary ion mass spectrometry.

Reflection high energy electron diffraction (RHEED) was observed *in situ* and used to monitor the film growth. The AlCrN films for the most part demonstrated 3D growth, as evidenced by spotty RHEED patterns. However, the AlCrN grown at T_{Cr} = 982°C demonstrated 2D growth with a pattern indicative of a 1x3 reconstruction (Figure 5), which was not observed for any other AlCrN films. Atomic force microscopy (AFM), a widely-used tool for investigating the topology of materials, was used to investigate the surface morphology of the AlCrN films. As expected from the RHEED patterns, the AlCrN films were considerably rougher than undoped AlN grown under similar conditions (Figure 6).

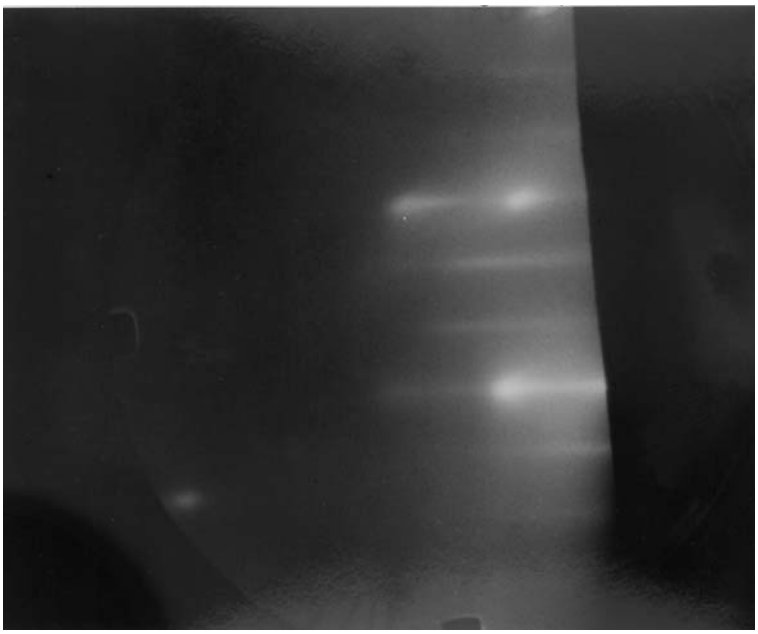

Figure 5. Reflection high energy electron diffraction photo of AlCrN film grown at a Cr cell temperature of 992°C.The photo depicts a 2D/3D pattern with one by three reconstruction.

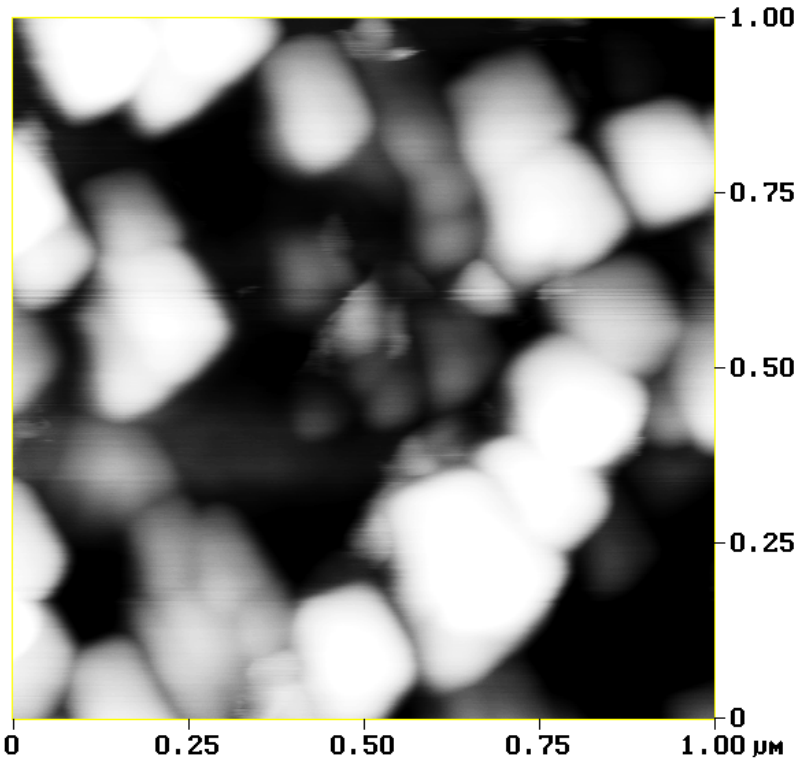

Figure 6. Atomic force microscopy image (1µm by 1µm) of AlCrN with an rms roughness value of approximately 11 nm.

Single phase and multi-phase AlCrN films were investigated. Powder x-ray diffraction was used to determine the phase composition of the films. The materials corresponding to T_{Cr} = 982-992°C were found to be single phase while material grown at T_{Cr} = 1005°C was found to contain multiple phases. Both Cr_2N and Al_xCr_y (most likely corresponding to Al_3Cr_2 and $AlCr_3$) were found in the higher Cr content film. High resolution x-ray diffraction was used to determine the lattice constant of the AlCrN films. As shown in Table 1, the lattice constant (a_0) of the single phase AlCrN was smaller than for AlN. This behavior was also observed in the similarly grown AlMnN films, as reported earlier in the chapter. The presence of second phases increased a_0 relative to the single phase films. A decrease in lattice constant with the introduction of a dopant indicates substitutional incorporation of the dopant. The rise in lattice constant with the presence of multiple phases suggests that more of the dopant is incorporating interstitially. The single phase AlCrN was found to be semi-insulating, while the multi-phase material was found to conduct via an electron hopping mechanism with activation energy for conduction of 0.19 eV. For non-optimized growth, second phases of Cr_2N and Al_xCr_y are produced in the AlN and the material is conducting (~1000 Ohm-cm), see Table 1.

The nitrogen flux was varied from 1.2-1.5 sccm in the growth of the AlCrN films to determine optimal V/III ratio. The significance of the V/III ratio lies in the relationship between incorporation of the transition metal ion and the resulting magnetization. Without a change in group III species or growth temperature, a change in group V species will affect the number of substitutional sites for dopants to occupy. At high V/III, however, the excess N at the surface may interfere with the transition metal incorporation, resulting in a reduction of the magnetic ordering. This results in an optimal V/III which will incorporate the maximum number of substitutional dopants. It follows that this will lead to the maximum magnetic signal arising from the substitutional dopants. Figure 7 shows the variation of the 300K saturation magnetization with respect to the flow rate of the nitrogen for the AlCrN films grown at T_{Cr} = 987°C. High N_2 flows appear to reduce the sticking coefficient of the Cr, resulting in a reduced Cr concentration and hence lower M_S.

The ferromagnetic signal was found to be much stronger in the optimized AlCrN film than in the optimized AlMnN film. Figure 4.8 compares the magnetization vs. applied field for the optimal AlCrN and AlMnN films. The signal strength of the optimized AlCrN is ~2.5 times that of the optimized AlMnN. This suggests that the ferromagnetic interaction in the AlN between the Cr ions is stronger than that of the Mn ions. The coercive fields of the AlCrN and AlMnN are nearly identical. This suggests that the domain structures of the materials are similar.

Strong ferromagnetism persists to 350K (the temperature limit of the SQUID magnetometer), in the optimized AlCrN. Moreover, the saturation magnetization remains unchanged in the temperature region from 10K-350K. By contrast, AlMnN films grown under similar conditions were found to decrease in magnetization at 300K as compared to 100K, as shown in Figure 1. This suggests that AlCrN has a Curie point above that of AlMnN. Moreover, the Curie temperature of AlCrN is well above room temperature whereas the Curie temperature of AlMnN is in the vicinity of room temperature. Another difference between the AlMnN and the AlCrN is in the shape of the magnetization vs. temperature trace. Interestingly, the "paramagnetic tail" seen in the AlMnN in the 10-50K region is less pronounced in the single phase AlCrN, as shown in Figure 9. This may be another indication of a stronger ferromagnetic interaction between Cr dopant ions and Mn dopant ions. Overall, Cr tends to be a better dopant than Mn in ferromagnetic AlN.

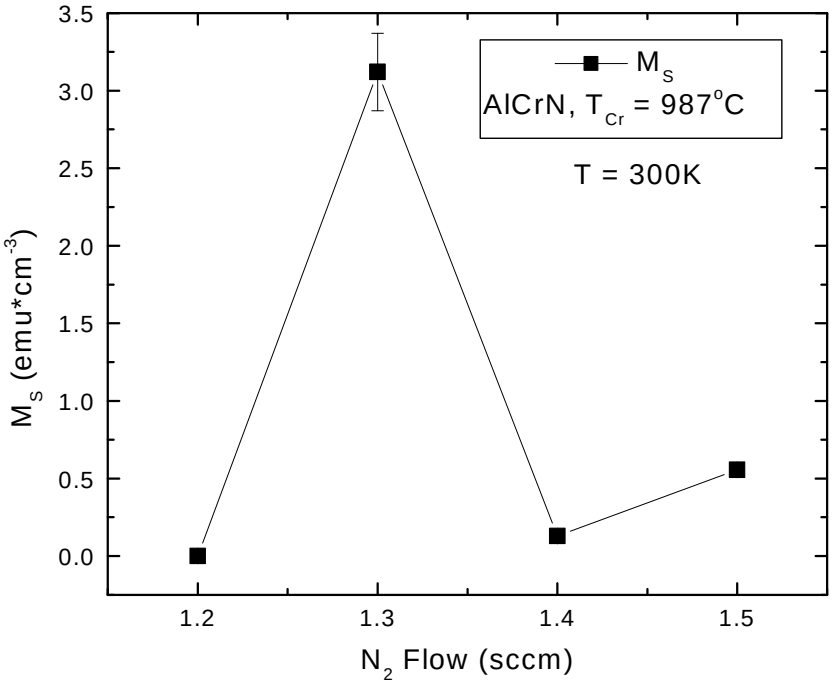

Figure 7. Magnetization versus nitrogen flow for AlCrN films grown at a substrate temperature of 780°C and with a Cr cell temperature of 987°C.

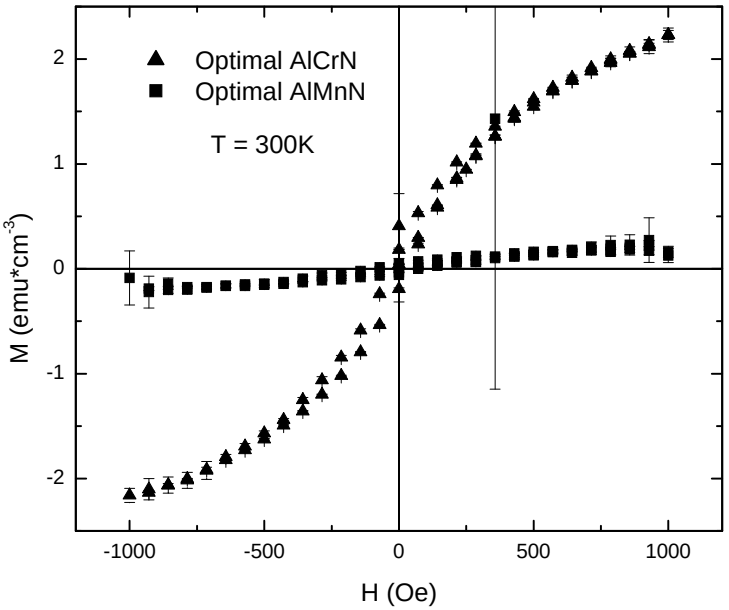

Figure 8. Magnetization vs. applied field for the optimal AlCrN and AlMnN films.

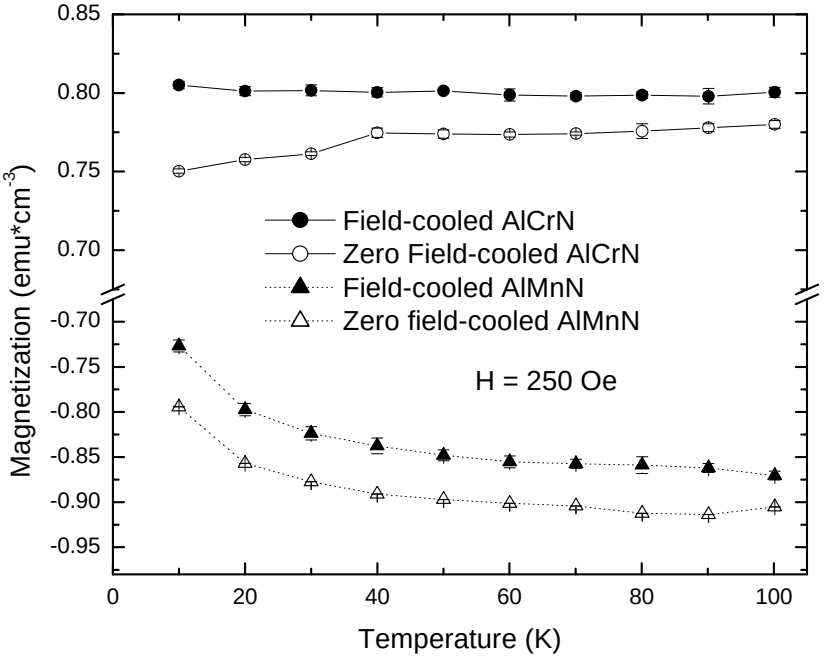

Figure 9. Magnetization vs. temperature in the temperature range from 10K-50K for AlMnN and AlCrN. A difference in curvature is seen for the two materials.

2.2 THERMAL STABILITY

The prospects for integrating a dilute magnetic semiconductor (DMS) into current technology depend upon the ability for the material to withstand certain chemical, thermal, and mechanical processes that occur during the processing of the thin film material into devices. Typically, III-N semiconductors are exposed to chemicals, in the form of solvents such as methanol and isopropyl alcohol, during the fabrication of devices including high electron mobility transistors (HEMTs) and light emitting diodes (LEDs). Standard procedures utilizing solvents are performed to mask the underlying material in order to provide a particular pattern to either remove the semiconductor or to deposit metal contacts. The strong bonding found in the III-Ns made these DMS resistant to such chemical exposure. However, some of the metal contacts to the III-Ns require a heat-activiating intermixing of various metal layers. This thermal anneal procedure is necessary to produce optimal electrical contact for III-N ohmics. Thermal anneal temperatures may easily exceed 700°C, or the low growth temperature required for III-N DMS growth. For this reason, it is necessary to investigate the thermal stability of DMS, to be certain that the material will withstand the elevated temperatures encountered during processing.

In order to effectively determine the material's thermal stability with respect to magnetic ordering, a systematic approach is applied. The magnetization of thin film epi-AlN DMS, is probed after a rapid thermal anneal at temperatures increasing in 100°C increments. The magnetization is extracted from SQUID measurements taken at 300K after each rapid thermal anneal (RTA) until no hysteresis is observed. The RTA temperature at which the magnetization is lost is taken to be the upper thermal limit of the material. In this manner, the thermal stability of III-N DMS may be systematically studied.

The optimal epi-AlCrN used in the investigation of thermal stability was grown at a substrate temperature (T_S) equal to 780°C with an Al cell temperature (T_{Al}) of 1150°C and a Cr cell temperature (T_{Cr}) of 987°C. The material was grown under a nitrogen plasma with a flow of 1.3 sccm. The AlCrN was annealed from 300°C-700°C in 100°C increments. Figure 10 shows the estimated saturation magnetization for each of the anneal temperatures. The estimated saturation magnetization was taken to be the magnetization at an applied field of 1000 Oe. From the as-grown condition (no anneal) to the initial anneal at 300°C, the magnetization decreases from 3.12 emu/cm^3 to 1.11 emu/cm^3. This drastic drop by almost a third indicates that the magnetic ordering is being affected by even a low temperature anneal at 300°C. The magnetization then decreases at the subsequent anneal at 400°C, nearly an order of magnitude below the as-grown value, but remains stable until T_{anneal} = 700°C. This indicates that the magnetic ordering is unaffected in the temperature range from 400°C up to nearly 700°C. However, at T_{anneal} = 700°C nearly all magnetic ordering is lost, as shown in Figure 11. The raw magnetization vs. applied field (M vs. H) after annealing at 700°C shows evidence of some hysteresis remaining, however the data is noisy and the loop is nearly flat implying that most of the magnetic ordering is destroyed by the 700°C anneal. The magnetization vs. temperature (M vs. T) before and after the 700°C anneal (Figure 12) corroborates the observation that the magnetization is lost as compared to the as-grown AlCrN. The noisy, yet consistently near zero, field-cooled signal is well below the signal obtained in the as-grown case.

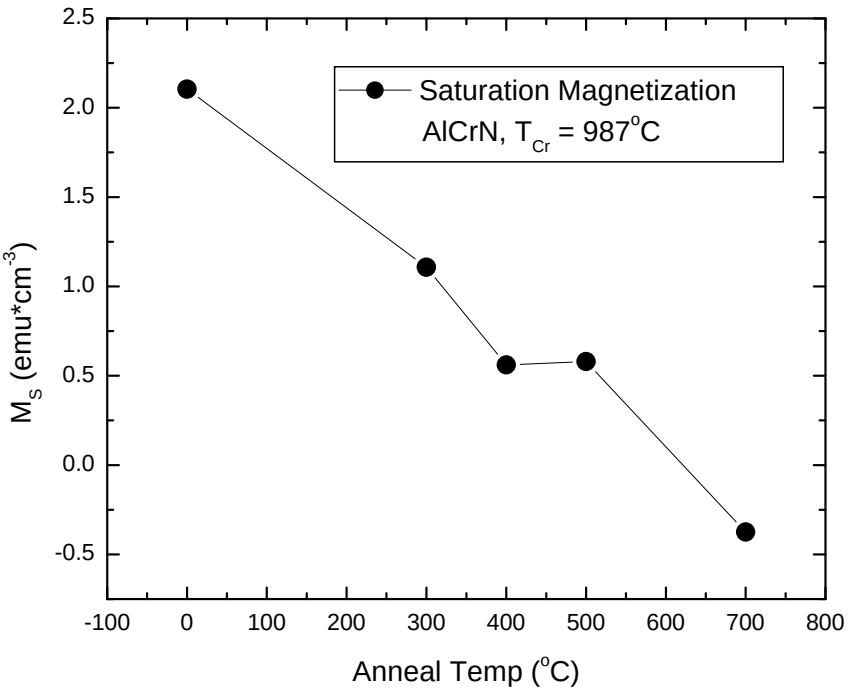

Figure 10. Estimated saturation magnetization for AlCrN at each anneal temperature.

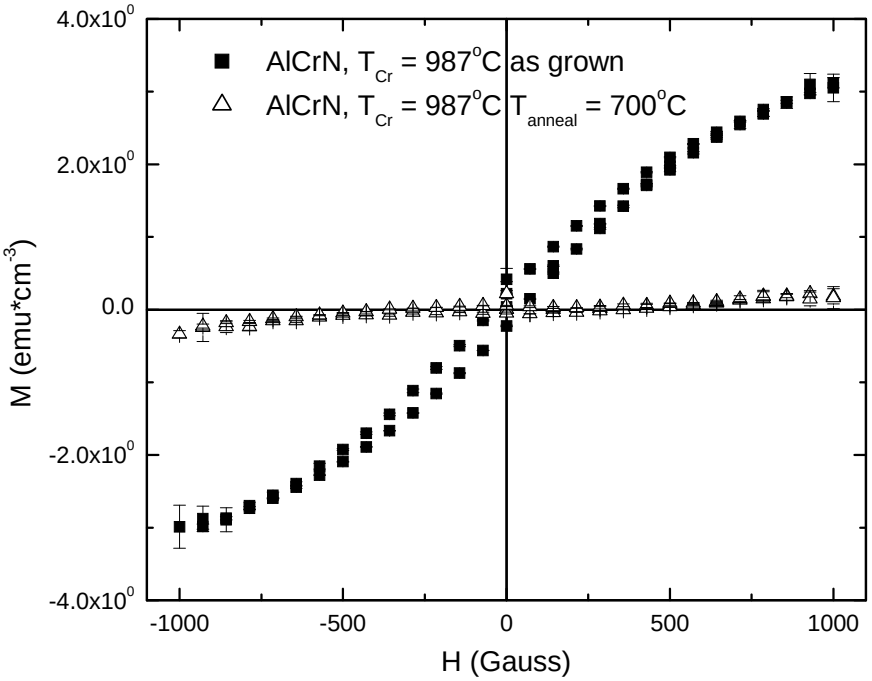

Figure 11. Magnetization versus applied field measurements comparing the as-grown AlCrN to the post-anneal AlCrN. Very little magnetization is left after an anneal of the AlCrN at 700°C.

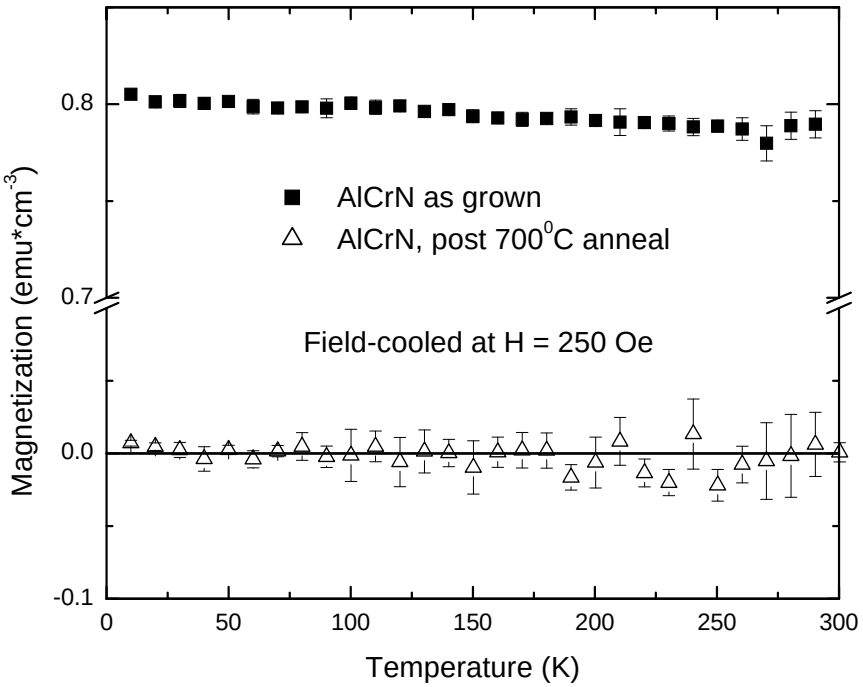

Figure 12. Magnetization versus temperature taken under an applied field of 250 Oe comparing as grown AlCrN to post-anneal AlCrN.

The upper limit of thermal resistance to magnetic degradation of the epi-AlCrN appears to be very near, yet lower than, the growth temperature of the material. The apparent discrepancy between the temperature at which the material's magnetic properties degrade and that of the magnetic properties of the as-grown AlCrN is explained as follows. During growth, active nitrogen species are delivered to the surface which is at elevated temperatures. This exposure to the active nitrogen species continues after growth during the cool down of the material. This is routine procedure which prevents the disassociation of nitrogen from the material while the material is still heated, ultimately resulting in no change of material during cool-down. However, during the RTA, the ambient gas is N_2, not the atomic nitrogen found in the plasma. It is plausible that during the anneal the quality of the AlCrN degraded due to the elevation of temperature without an atomic nitrogen overpressure, which lead to the loss of nitrogen and degradation of magnetic ordering. The extent of degradation could range from slight deterioration in crystallinity of the AlCrN to destruction creation of second phases.

The investigation of the AlCrN material phase after the 700°C anneal would give a clear indication of phase degradation. Figure 13 shows the powder x-ray diffraction (XRD) scans of AlCrN before and after the anneal at 700°C. No second phases are observed after the 700°C anneal. The main difference between the XRD scans is the broad peak around 20 degrees, which corresponds to the substrate, and gives no insight into the epi layer. The absence of second phases implies that the extent of material degradation from the anneal is not sufficient enough to change the phase of the material. However, as seen in the SQUID data, the effect of a 700°C anneal leads to a degradation of magnetic properties.

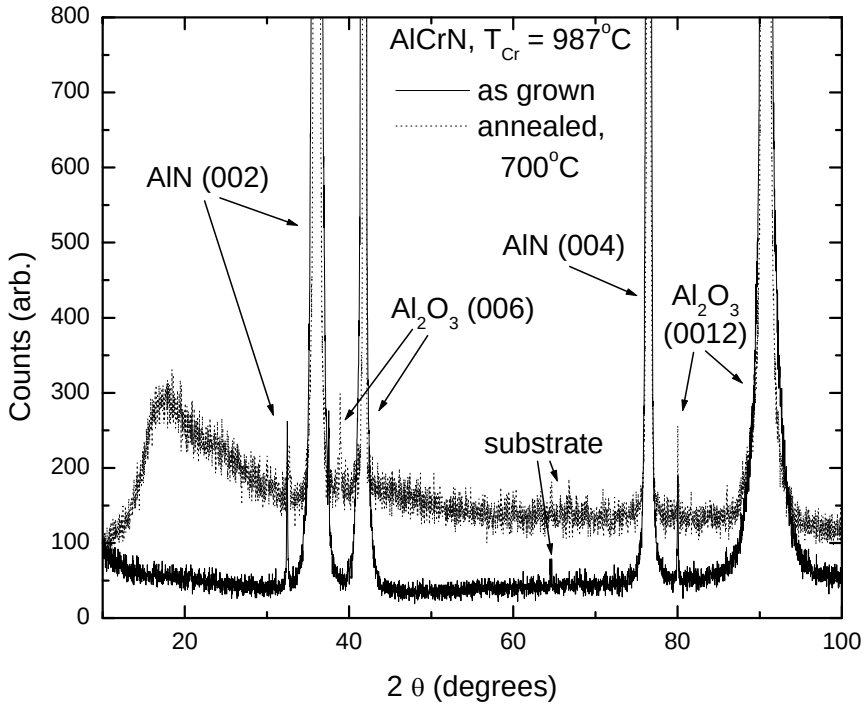

Figure 13. Powder x-ray diffraction scans comparing as grown AlCrN to post-annealed AlCrN. No second phases are apparent after the 700°C anneal.

The thermal stability of optimal epi-AlCrN was investigated and was found to be poorer than that of GaCrN. The upper limit of anneal temperature before destruction of magnetic

properties was found to be 700°C. No indication of second phases was observed after the 700°C anneal, which implies that the RTA was not significant enough to destroy the single phase AlCrN. However, although the single phase AlCrN withstood the RTA, the magnetic interaction within the material did not. This suggests that the mechanism for magnetization within this particular DMS is too weak to endure routine processing procedures during fabrication, such as the annealing of ohmic contacts. Hence, processing procedures must be altered for incorporation into current technology or alternate materials will need to be used in place of AlCrN.

2.3 ALN AND GAN BASED DILUTE MAGNETIC SEMICONDUCTOR APPLICATIONS

The most obvious application of an AlN-based DMS into an active device is by its use as a ferromagnetic barrier. A ferromagnetic insulator shows promise as a spin filter by allowing tunneling of aligned electrons and preventing tunneling of antiparallel electrons. The effect is a change in resistance with applied magnetic field and is dubbed tunneling magneto-resistance (TMR). For example, EuS was used as a spin filter and showed evidence of magnetoresistance (MR) exceeding 130% at temperatures below the Curie temperature of the material (~70K). AlN has the potential of being applied in the same manner, however with an operable device at room temperature, since the Curie point is above 300K.

The all semiconductor device structure schematic is shown in Figure 14. Two device stacks were grown, one with a ferromagnetic insulator and a reference with a non ferromagnetic insulator. The tunneling magneto-resistance (TMR) stack includes two ferromagnetic layers: a spin injector which serves to provide electrons with aligned spin states and a spin filter which controls the amount of charge transport via tunneling. The reference stack contains only one ferromagnetic layer, the spin injector. In the case of the TMR stack, tunneling is expected to increase if both the spin injector and spin filter are magnetically aligned by the application of an external magnetic field. However, in the case of the reference device, there is no change expected in tunneling with the application of an external magnetic field.

In the TMR stack, optimal GaMnN was used as a spin injector and optimal AlMnN was used as a spin filter. In the reference stack, the AlN was grown under the same conditions as the TMR stack, but without the addition of Mn. Both structures were grown on an MOCVD-GaN buffer from the same wafer, which was chemically pretreated with a 3 minute 1:1 HCl:H_2O dip, a 25 minute UVO_3 exposure, and a 5 minute BOE dip followed by a DI rinse and N_2 dry. The substrate was heated in situ under N plasma to 700°C before growth and a streaky RHEED pattern was obtained prior to growth to ensure a clean growth surface. A 50 nm thick GaN:Si layer was grown, followed by a 7.5 nm AlMnN layer (AlN, for the reference stack). The GaMnN spin injector was 10 nm thick and another 50 nm GaN:Si layer was grown to provide better electrical contact to the ohmics.

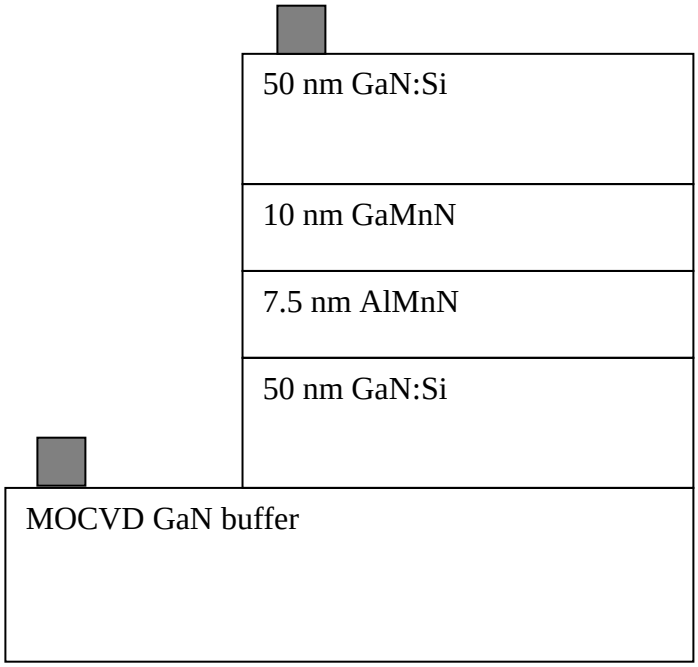

Figure 14. Schematic of the all semiconductor tunneling magneto-resistance stack. The reference stack contained undoped AlN in place of the AlMnN layer, and all thicknessed remained the same. The dark squares represent ohmic contacts made to the top GaN:Si layer and to the underlying MOCVD GaN buffer.

The devices were then fabricated into thin bars with large area contact pads on each end. The mask design is shown in Figure 15. The bar bell type structures allow for incorporation of anisotropic ferromagnets such as Co, for which the aspect ratio of 10:1 would force the coercive field to higher values. This shape is useful for creating large differences in the values of the coercive fields to separate magneto-resistance maxima in measurements. The devices were fabricated using standard photolithography to pattern and etch mesas via ICP and to pattern then evaporate ohmic contacts. An SEM image of the fabricated all semiconductor TMR device is shown in Fig. 16. Ohmic contacts consisted of 50 nm Ti and 500 nm Au. Ohmic contacts were not annealed to improve contact resistance due to the thermal instability of the DMS.

Electrical and magneto-resistance measurements were performed to determine the functionality of the devices. All measurements were done on both the TMR stacks and the reference stack. Room temperature current-voltage (I-V) measurements of the TMR stack without an applied magnetic field and with an applied magnetic field compare device operation in the randomized state vs. device operation in the parallel state. Figure 17 shows an increase in slope and exponential behavior of the TMR device after an applied field of H = 4000 Oe. The device in the randomized state shows less of the expected tunneling behavior (as indicated by the decrease in slope). This suggests that the tunneling increases when the GaMnN and AlMnN are aligned, which agrees with the expected operation of the device. The room temperature I-V measurements provide a useful survey method to determine the promise of the device.

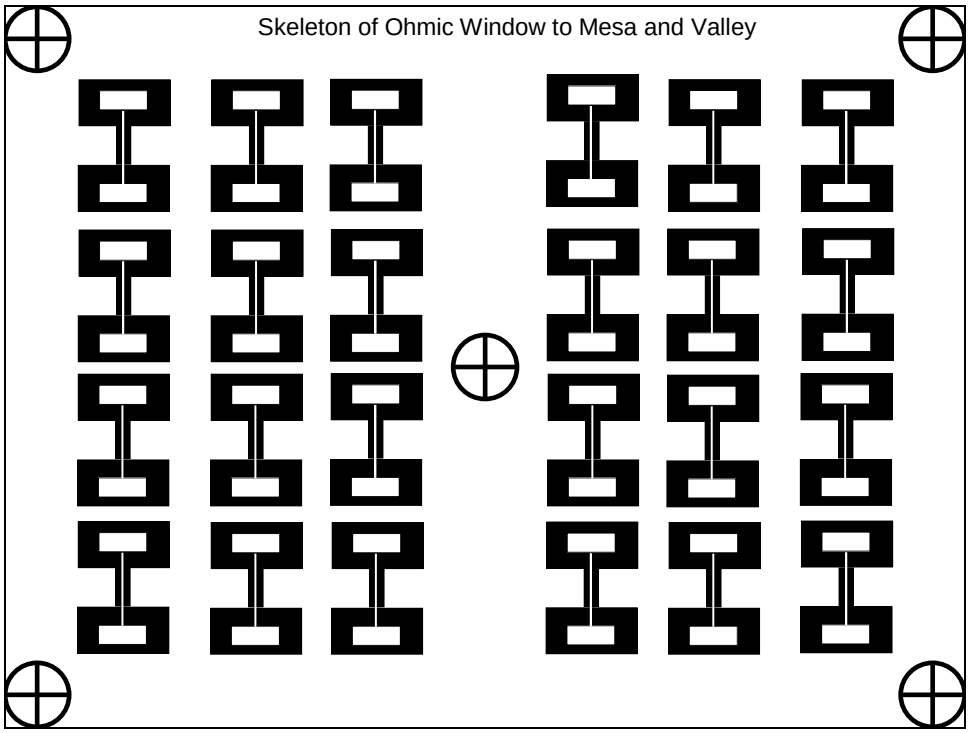

Figure 15 Mask design used for fabrication of all semiconductor device. Alignment marks are found at each corner and in the middle of the mask. The larger dark bars represent the area of the mesa of the device. The open, or light areas, represent where ohmic contact was made to the device.

Magneto-resistance (MR) measurements were performed in a Quantum Design Physical Properties Measurement System (PPMS) by measuring the resistance of the samples while sweeping an applied magnetic field. The PPMS measurements are limited to a maximum of 95 mV and 999μA. These restrictions hinder measurements of highly resistive material. The room temperature measurement of the reference sample showed no change in resistance with respect to the magnetic field. This complies with the expected behavior with no spin filter. The resistance vs. applied magnetic field (R vs. H) at 5K is shown in Figure 18 for the reference device. A slight change in resistance appears at high field, which most likely comes from the small change in resistance of the GaMnN. Since the change is so small, it is most likely due to the thin spin injector's inherent magnetoresistance. The origin of the splitting of resistances between 3000 Oe to -500 Oe and on the up sweep between -500 Oe to 3000 Oe is unknown. However, the same splitting is found in the R vs. H of the TMR device at 300K, shown in Figure 19. No MR can be seen at 300K in the TMR device. Comparison measurements at 5K could not be performed due to the high contact resistance found in the TMR device at low temperature.

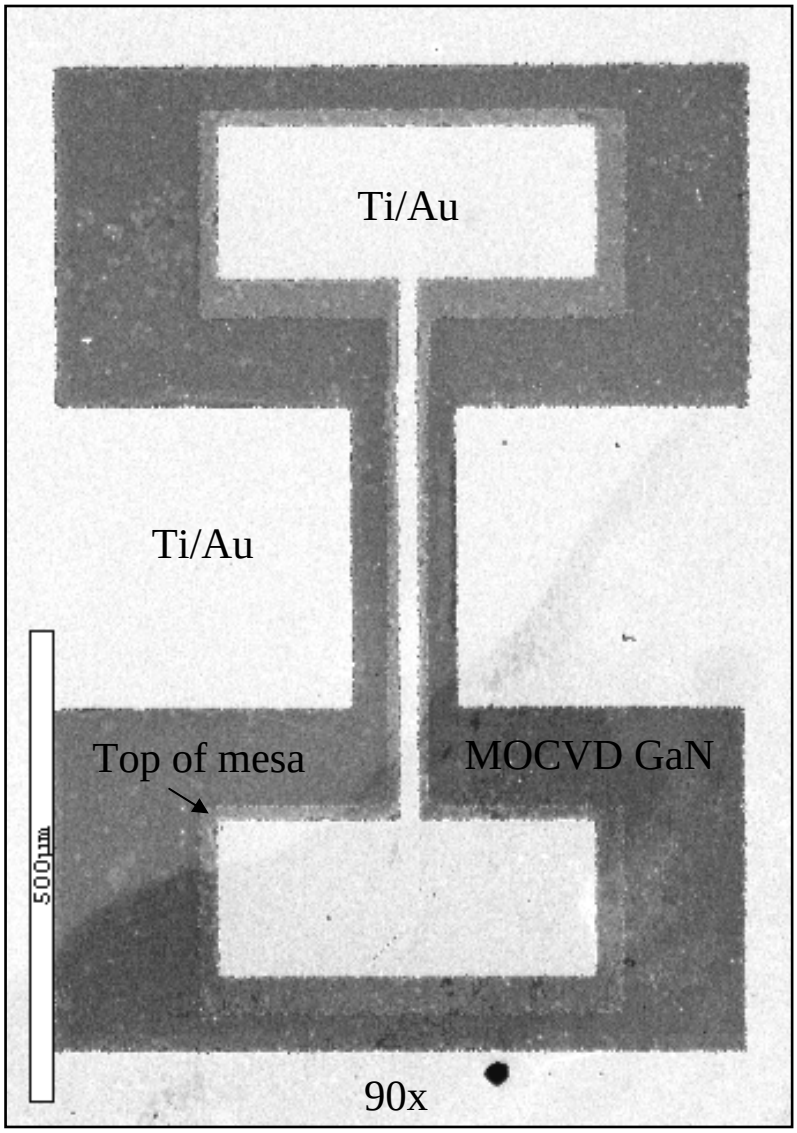

Figure 16. Scanning electron micrograph of all semiconductor device. Top view shows top and bottom Ti/Au ohmic contact, the top of the mesa and the etched valley showing the MOCVD GaN buffer.

Structural investigation of the TMR device was performed by TEM of the cross section of the device to determine the growth quality at the interfaces. Fig. 20 is a dark field image where the TRM layers can easily be seen. Interfacial roughness between the GaN:Si and the AlMnN layer is evident by the wave-like shape of the AlMnN layer. Upon closer examination of the AlMnN layer, defects can be seen (Fig. 21). This indicates that the growth of the device is not optimized, and is a plausible reason for the inability of the device to operate as expected at room temperature.

In summary, room temperature I-V measurements showed promising results for the TMR device. Tunneling increased when the spin injector and spin filter were aligned, as compared to the randomized state. However, PPMS measurements were not quite so promising, in that no

TMR was observed at room temperature in the TMR device. Unfortunately, due to the limits of the PPMS, no MR measurements could be made at low temperature. Through TEM imaging, high amounts of strain were observed in the AlMnN spin filter. This is one possible reason for no MR at 300K. Another possibility is that the Mn impurity introduces impurity bands into the DMS. This distribution of levels may cause the MR to be less defined.

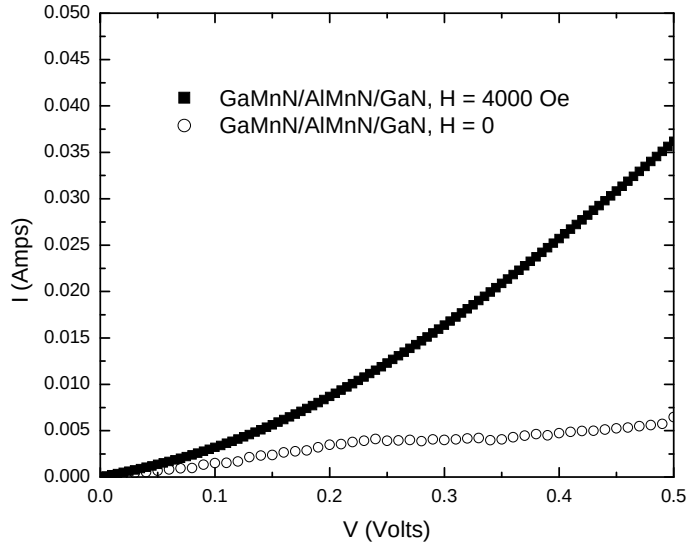

Figure 17. Current-voltage measurement of all semiconductor tunneling magneto-resistance device with and without and applied magnetic field. Open circles represent the I-V measurement taken without an applied field. Dark squares represent I-V measurement taken after application of a 4000 Oe field. Note that tunneling increases after the field is applied.

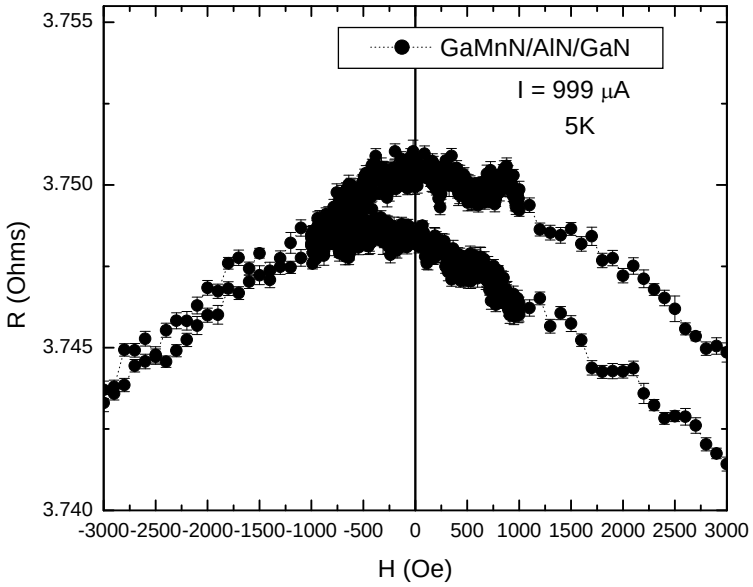

Figure 18. Resistance vs. applied field measurement taken at 5K for the all semiconductor reference device.

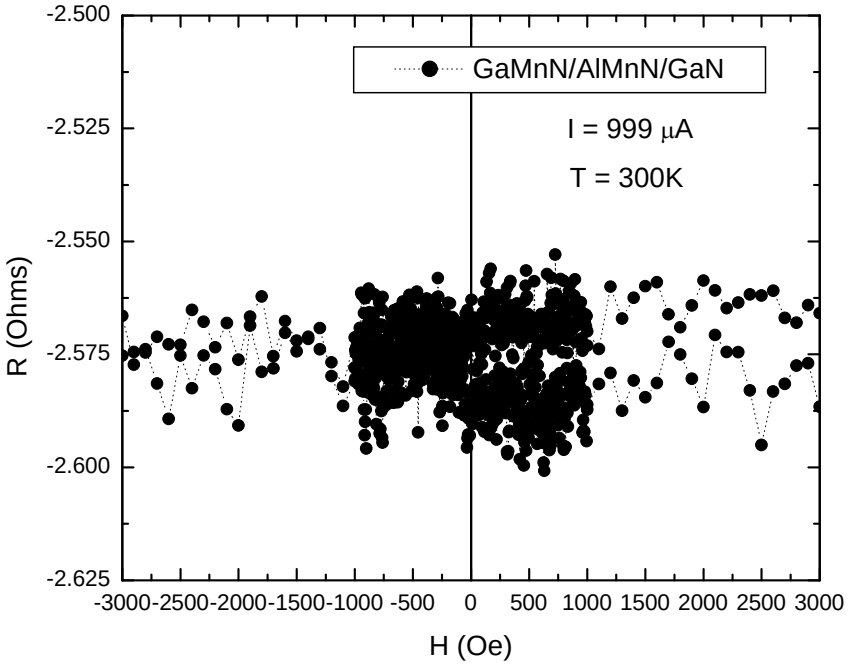

Figure 19. Resistance vs. applied field taken at 300K for the all semiconductor tunneling magneto-resistance device.

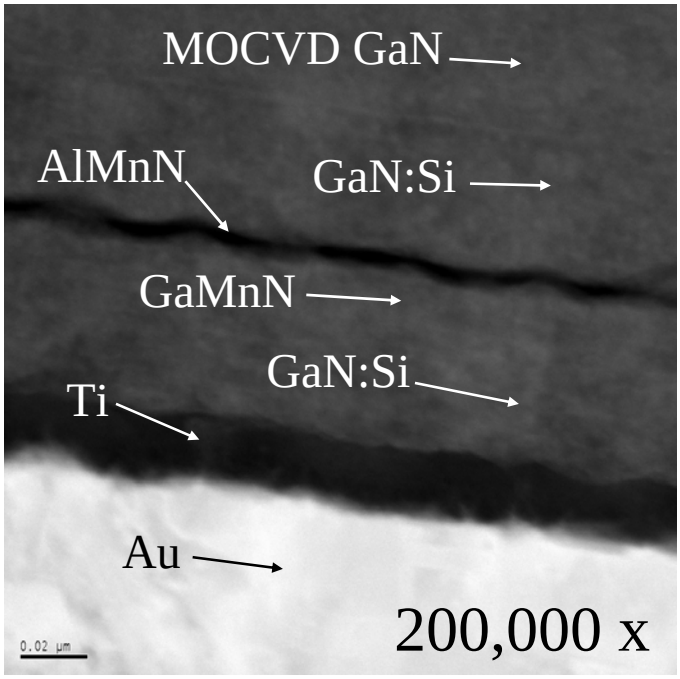

Figure 20. Dark field ZSTEM image taken of the all semiconductor tunneling magneto-resistance device. The dark AlMnN layer shows roughness indicating poor growth quality at the interface.

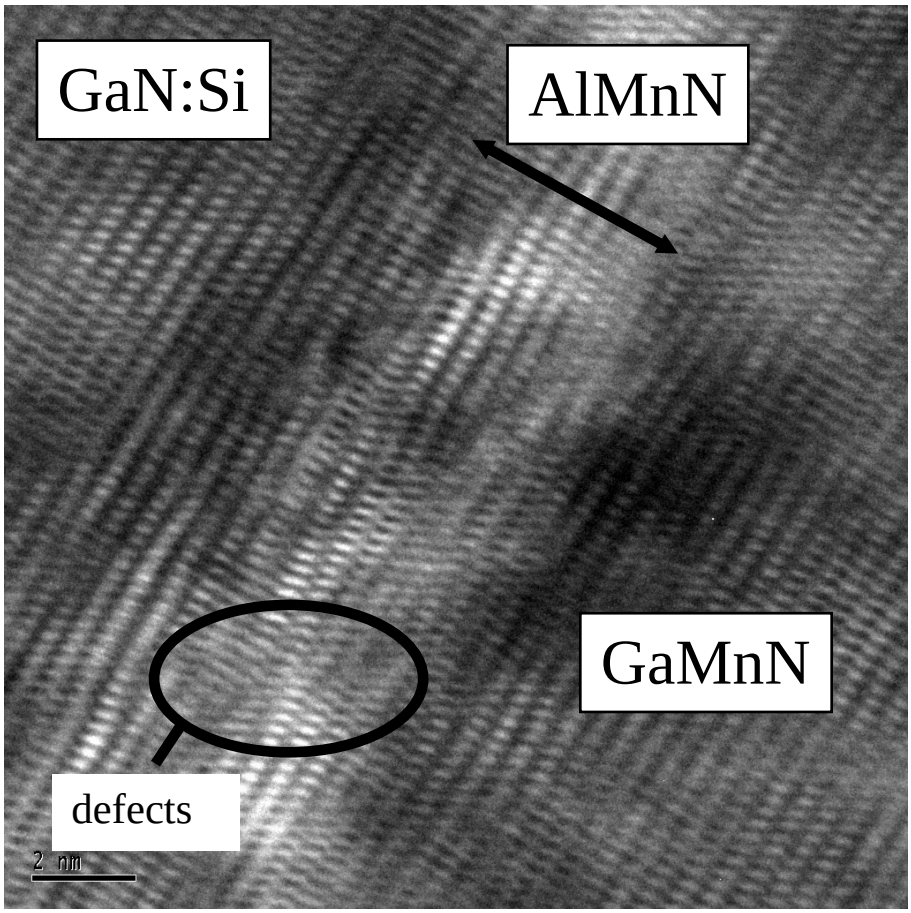

Figure 21. Selected area diffraction pattern tunneling electron micrograph taken of the all semiconductor tunneling magneto-resistance device. The AlMnN spin filter layer is indicated with an arrow. Strain can be seen within the AlMnN layer as indicated in the photo.

Other spin injectors were also grown, namely FeNi and MnAs, which replaced the GaMnN in the TMR stack. FeNi did not withstand the photolithography, and oxidized and degraded before testing was accomplished, see Figure 22. The MnAs survived processing, but was too soft for wire bonding, making MR measurements impossible. Improvements on TMR devices can be made by using alternative tunnel layers which contain an impurity level instead of impurity distribution. One such promising impurity is Gd, which would allow for a single impurity level in III-N DMS.

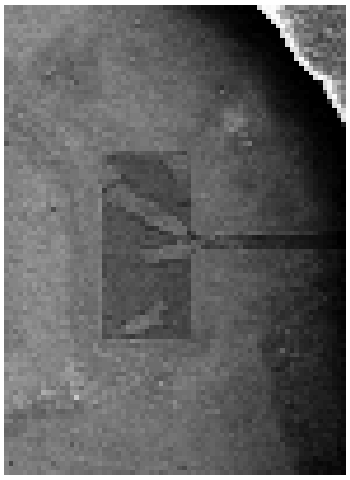

Figure 22. Scanning electron micrograph of a tunneling magneto-resistance device with FeNi as a spin injector. From the photo, the degradation of the FeNi is visible on the contact pad. This degradation represents nearly 90% of the devices. The FeNi degraded during photolithography, most likely due to the use of solvents during processing.

2.4 INVESTIGATION OF GADOLINIUM AS A MAGNETIC DOPANT

There is continued strong interest in the properties of rare-earth-doped wide band gap nitrides for their potential application in optoelectronic devices such as visible lasers that can be grown on Si substrates.[1–20] Rare earth doping of GaN with Eu and Gd has been reported to produce ferromagnetism, although the mechanism is far from clear.[21–26] Several groups have suggested that there is long range polarization of the area surrounding each Gd atom.[23,24,27] Dalpian and Wei[27] further suggested that the phenomenon requires shallow donor impurities such as oxygen to occupy f states created by the Gd below the conduction band. However, there is a significant difference in the dopant concentrations needed to induce ferromagnetism in GaN between rare earths and the more conventional transition metals such as Mn. In the latter case, concentrations of 3–5 at.% are typically required and this is well above the solid solubility, requiring use of low growth temperatures or nonequilibrium incorporation methods such as ion implantation. By comparison, concentrations of 10^{16}–10^{18} cm^{-3} of Gd and Eu appear sufficient to induce ferromagnetism and correspondingly large magnetic moments. This has the advantage that there is less compromise in the material quality through the use of lower impurity levels and the material may be codoped with conventional shallow level dopants to control the conductivity. Since the rare earth dopants may be optically active in these materials, magnetic and optical functionalities on a single chip may be possible. For this reason, the magnetic properties of epitaxial GaN doped with Gd are explored.

Epitaxial GaN doped with Gd was grown by gas source molecular beam epitaxy (GSMBE). Samples were grown on metalorganic chemical vapor deposition (MOCVD) GaN buffers, chemically treated prior to growth with the standard preparation discussed previously. The substrates were heated to 700°C under 1.6 sccm nitrogen plasma before growth to verify a streaky reflection high energy electron diffraction (RHEED) pattern, which indicates a clean growth surface. During growth initiation, the substrates were first exposed to Ga and N, before

the Gd shutter was opened. Each of the GaN:Gd samples was grown at a substrate thermocouple reading (T_S) of 700°C, a Ga cell temperature (T_{Ga}) of 785°C and a nitrogen plasma flow of 1.6 sccm. The Gd cell temperature (T_{Gd}) was varied between 900°C-1125°C.

RHEED was used to monitor the growth in situ. Samples corresponding to T_{Gd} = 900-950°C demonstrated spotty (3D) RHEED patterns. GaN:Gd grown at T_{Gd} = 1050°C demonstrated 2D/3D RHEED patterns with a 1x3 reconstruction. Figure 23 shows the 1x3 reconstruction observed during growth of the GaN:Gd. Atomic force microscopy (AFM) was used to investigate the roughness of the films after growth. An AFM image of Gd-doped GaN is shown in Figure 24 for TGd = 950°C. The rms roughness value was 2.934 nm, which was typical for all GaN:Gd.

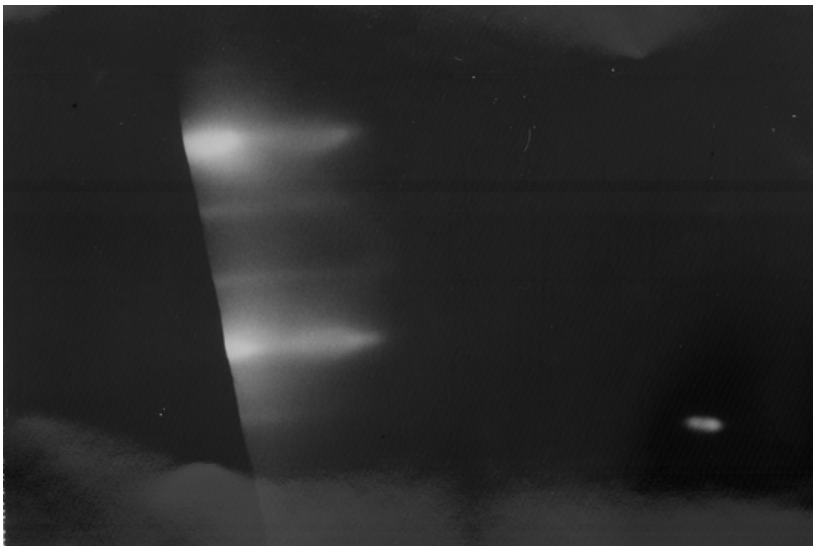

Figure 23. Reflection high energy electron diffraction pattern of GaN:Gd, T_{Gd} = 1050°C. The picture shows a 2D/3D pattern with 1x3 reconstruction.

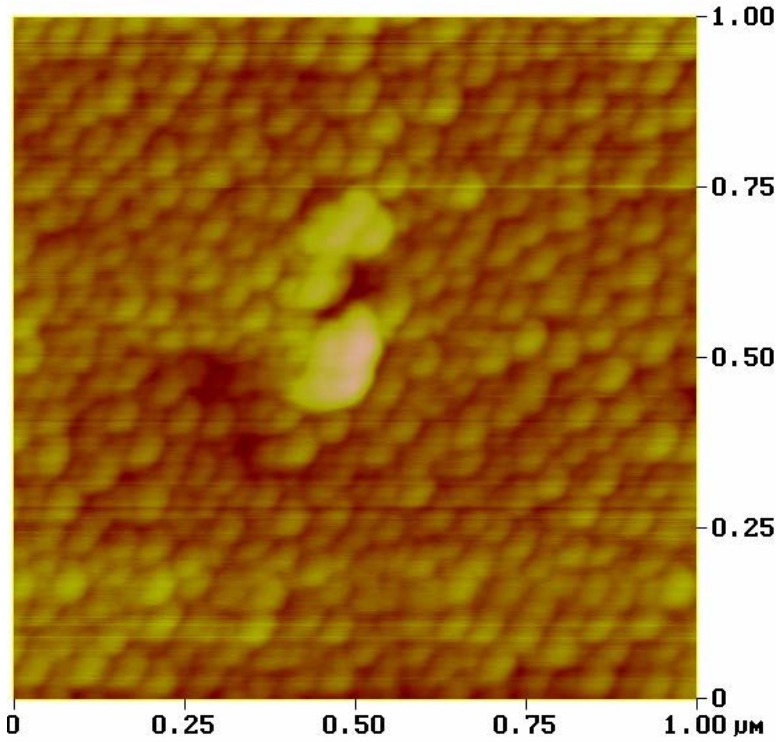

Figure 24. Atomic force microscopy image representing GaN:Gd with rms roughness of 1.541 nm.

Magnetization vs. applied field (M vs. H) was scanned for each of the GaN:Gd samples. For T_{Gd} = 900°C, no hysteresis was observed at any temperature. At T_{Gd} = 950°C, ferromagnetism is observed at 50K, as shown in Figure 25. However, the magnetization level is very low at 50K and becomes noisy and questionable at 300K and 350K. For T_{Gd} in the range of 1000°C-1100°C, ferromagnetism is clearly evident in the M vs. H loops. Figure 26 shows the M vs. H loops at 50K for the samples corresponding to T_{Gd} = 1000-1100°C. At TGd = 1125°C, there is no evidence of ferromagnetism in GaN:Gd at 50K, 300K, or 350K. Therefore, the Gd cell temperature range of 100°C yields ferromagnetism in GaN:Gd.

A comparison of the estimated saturation magnetization (corresponding to the magnetization at 1600 Gauss) depicts the dependence of ferromagnetism on T_{Gd}. The optimal Gd condition is T_{Gd} = 1050°C, as shown in Figure 27. This trace of M_S and M_R at 300K vs. T_{Gd} implies that there is a certain amount of dopant which yields the maximum magnetization. This behavior is similar to that found for the transition metal dopants, Mn and Cr. However, unlike the transition metal dopants, the Gd incorporation is at a much lower level. The flux readings for Mn and Cr during growth are on the order of 10^{-8}, but the Gd flux reading is much lower, below 10^{-10}. The presence of an optimal cell temperature for the transition metals can be attributed to the concentration level and incorporation site of the dopants. At too low of a cell temperature, not enough dopant is incorporating substitutionally which results in a low magnetization level. At too high a cell temperature (corresponding to a few atomic percent dopant) the transition metals begin to occupy interstitial sites which results in a degradation of the magnetic interaction. However, in the case of Gd, it is not probable that the amount of Gd incorporated

into the GaN can be high enough for the Gd to incorporate interstitially. Therefore, a different mechanism must be driving the magnetization in GaN:Gd.

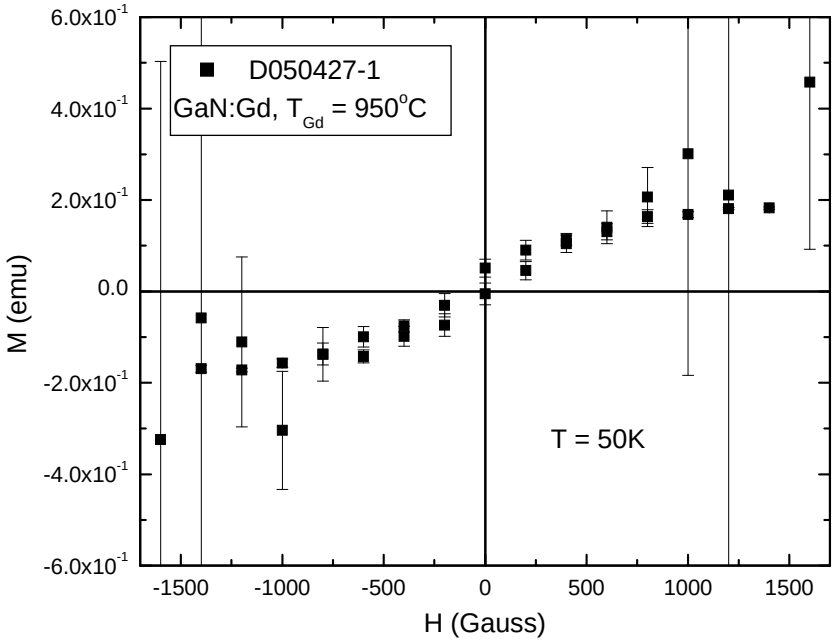

Figure 25. Magnetization vs. applied field loop taken at 50K for GaN:Gd, with T_{Gd} = 950°C. Hysteresis is observed at 50K, but not necessarily at 300K or 350K.

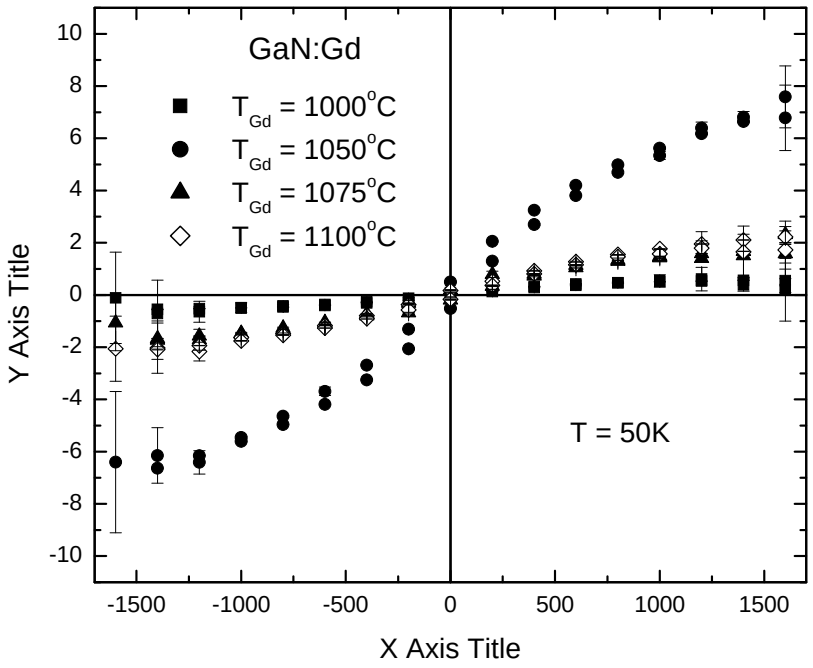

Figure 26. Magnetization vs. applied field taken at 50K for GaN:Gd corresponding to T_{Gd} = 1000°C-1100°C.

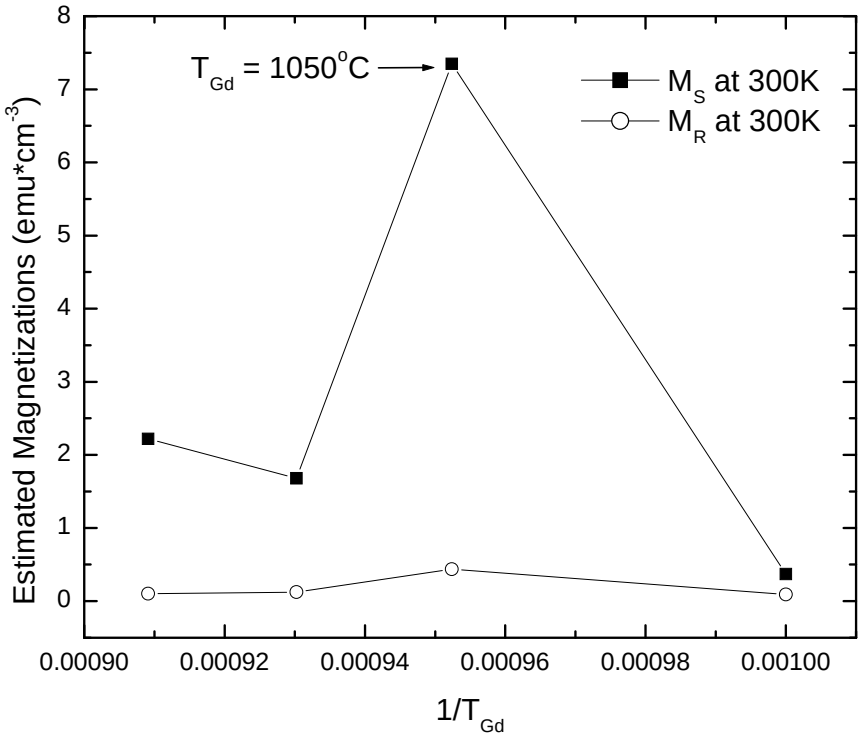

Figure 27. Estimated saturation magnetization vs. inverse of Gd cell temperature plot which shows the optimal T_{Gd}.

The magnetization vs. applied field for T_{Gd} = 950°C was found to decrease from 50K to 350K. However, this behavior was not observed at higher T_{Gd}. Figure 28 shows the M vs. H loops at T = 50K, 300K, and 350K for T_{Gd} = 1050°C. The magnetization appears stable from 50K to 350K for T_{Gd} = 1050°C as indicated by the loops. However, the magnetization vs. temperature (M vs. T) seems to indicate a decrease in magnetization, as shown in Figure 29. The zero field-cooled and field-cooled traces are widely separated until near room temperature. The instability around room temperature may be a sign that this temperature is in the vicinity of the Curie point (T_C) of the material. This behavior is reminiscent of that of bulk Gd, which has a T_C ~ 300K. Conversely, the magnetization of the transition metals (which are antiferromagnetic) do not correspond to the magnetization in III-N:TM. This is yet another indication that there is a different mechanism of ferromagnetism in the GaN:Gd.

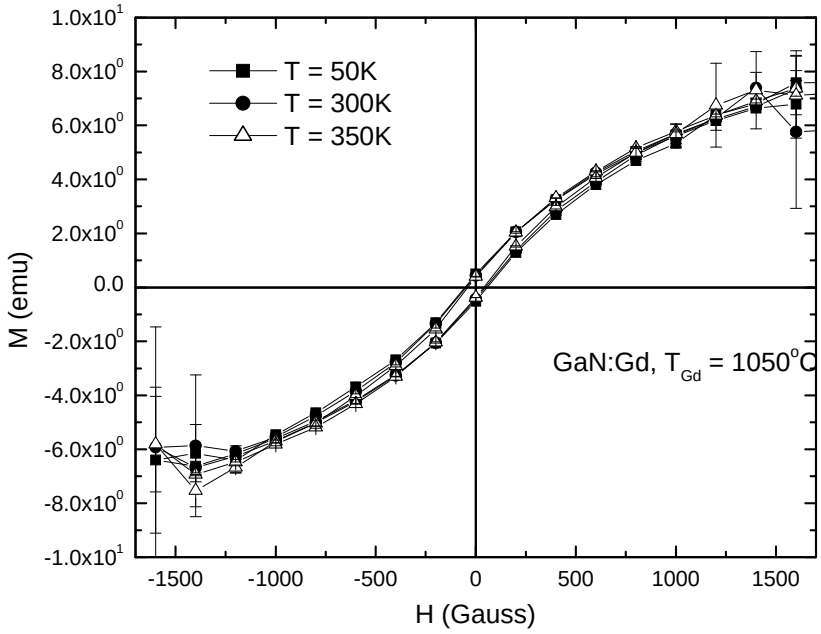

Figure 28. Magnetization vs. applied field loops taken at 50K, 300K, and 350K for GaN:Gd with T_{Gd} = 1050°C.

To investigate impurity concentration effects in the material, a series of growth runs varying the Gd cell temperature from 950 to 1125ºC were performed in films ~0.15μm thick. The concentration of Gd within the films was investigated via secondary ion mass spectroscopy (SIMS). Similar to a report by Dhar et al., this concentration was extremely low, falling under the SIMS background level of 10^{17} atoms/cc. The oxygen content in these samples was on the order of 10^{19} atoms/cc. These films are extremely resistive, and immeasurable by our Hall systems. Comparing this with carrier concentrations of our undoped MBE grown GaN in the order of 10^{16} cm^{-3}, it can be reasoned that the Gd has to contribute a concentration on the same order.

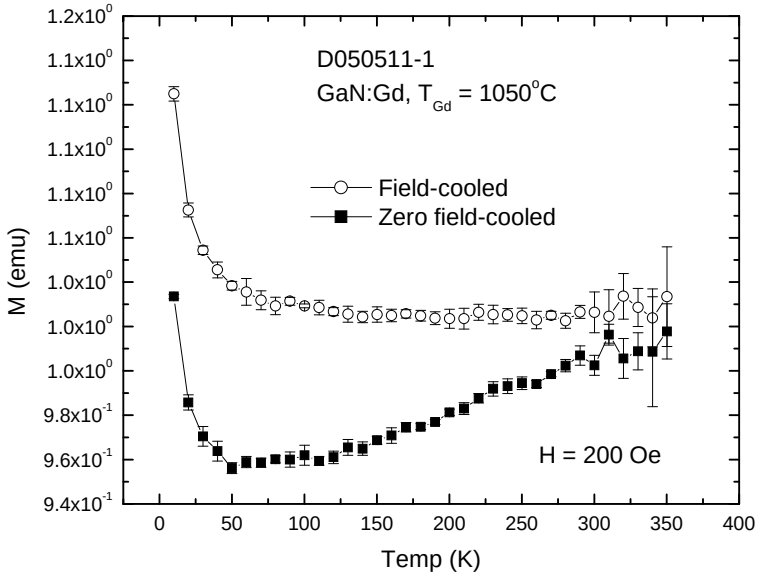

Figure 29. Magnetization vs. temperature for GaN:Gd with T_{Gd} = 1050°C. Note that the magnetization is significantly decreased near room temperature.

Even with this low concentration of Gd, the films exhibited hysteresis at room temperature. A maximum in magnetic saturation (M_S) was found at T_{Gd} = 1050ºC, as seen in Figure 30, coinciding with the best RHEED pattern. Hysteresis completely disappeared for cell temperatures above 1100ºC, so they are not included in the figure. This pattern of M_S peaking over a certain temperature or concentration range has been seen in other GaN doped DMS materials.

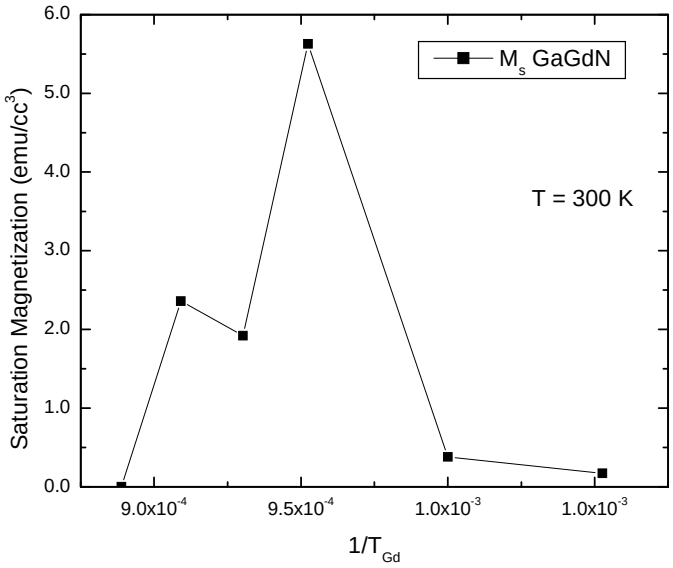

Figure 30. Saturation magnetization vs. Gd cell temperature for GaGdN taken at 300 K. Saturation magnetization taken at an applied field of 1000 Gauss from magnetization vs. applied field measurements.

To rule out interface effects as the source of ferromagnetism in the samples, GaGdN films were grown at thicknesses varying between 0.1μm and 0.6μm, at T_{Gd} = 1050ºC. If interfacial effects were influencing the ferromagnetism, then the magnetic signal as a function of volume should steadily decrease with increasing film thicknesses. This is clearly not the case, as shown in Figure 31. The high degree of magnetism seen in the 0.1μm thick film has been repeated, and can be attributed to better crystal growth, as increasing thickness corresponded with a trend towards three dimensional growth. The measured coercivity for these films stayed fairly constant with measured values between 38.5 and 43.17 Oe, also shown in Figure 31. Dhar et al have stated a similar conclusion using magnetic signal per area to report thickness independence.

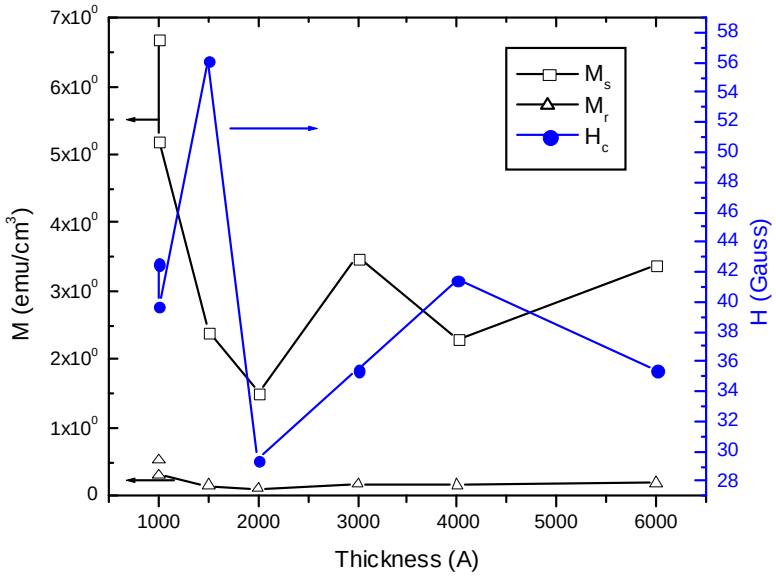

Figure 31. Saturation magnetization, coercivity, and remnant magnetization vs. film thickness taken at 300 K. Saturation magnetization taken at an applied field of 1000 Gauss from magnetization vs. applied field measurements. Coercivity and remnant magnetization also read from magnetization vs applied field measurements.

These films also suggest they have T_Cs beyond room temperature, as shown by the absence of change in hysteresis at high and low temperature in the magnetization vs. applied field curves for the GaN:Gd films, which is shown for a 1000Å film in Figure 32. The magnetization vs. temperature shown in the inset of Figure 32 supports the same conclusion as evidenced by the lack of closure between the field cooled and zero field cooled lines.

The mechanism behind the ferromagnetism of this system is still under consideration. It does not follow free carrier mediated theory due to the high resistivity of the material. Dhar *et al* and Dalpain *et al* have recently proposed models to explain the ferromagnetism in this dilute doped system, both of which are based on long range polarization of the area surrounding each Gd atom. However, Dalpain has suggested the phenomenon requires shallow donor impurities to occupy *f* states created by the Gd below the conduction band. This is interesting, especially noting the high concentration of oxygen noted in both our films and those of Dhar *et al*. These

models also allow for the signal peak seen in Figure 30 due to overlapping Gd spheres of influence, and the decline in moment at higher Gd cell temperatures/concentrations.

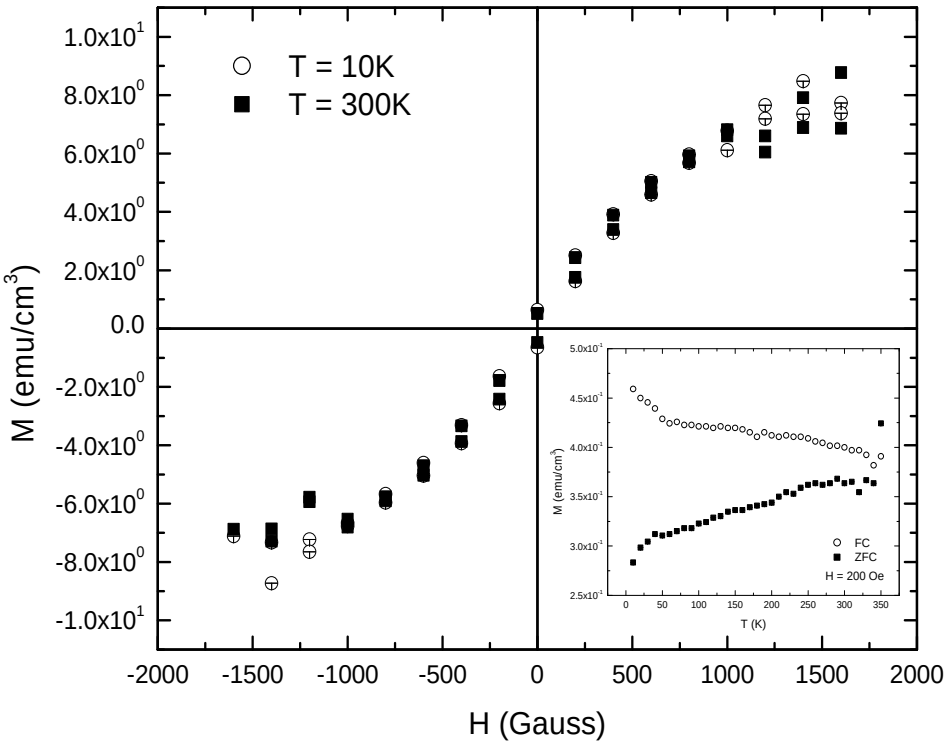

Figure 32. Magnetization vs. applied field at 300 K and 10 K for an 1000Å thick GaGdN film, grown at T_{Gd} = 1050ºC shown at top. The inset shows magnetization vs. temperature at an applied field of 200 Oe showing both field cooled and zero field cooled traces.

Co-doping with Gd and Si was carried out to see if extra shallow donors would affect the ferromagnetism of the material. The films were grown at T_{Si} between 1000 and 1200°C and a thickness of 0.15μm. Two dimensional growth with 1x3 reconstruction was recorded and resulted in conductive n-type material. At T_{Si} = 1000°C, the material was still slightly resistive, but carrier concentration markedly improved from there, increasing an order of magnitude with each 100°C change, reaching 1.45 x 10^{18} cm^{-3} with the highest concentration of Si. Meanwhile, the Hall resistivity dropped to 0.04 Ω-cm. As shown in Figure 33, the magnetic saturation and remnant magnetization increase linearly with cell temperature, while the coercivity shows the opposite trend. The coercivities of the co-doped material are in within the same values, but in a smaller range than those of the purely Gd-doped films. Remnant magnetization for the higher T_{Si} films is comparable to the 1000Å thick GaN:Gd films. The value of paramount interest, though, is the high M_S value found in the co-doped material above 1000°C. For the film grown at T_{Si} = 1100°C, the Ms is in the range of the 1000Å thick GaN:Gd films, and at the higher cell temperature, the saturation magnetization far outstrips any of the purely Gd-doped films. Looking into the hysteresis loops of the 1200°C T_{Si}, the change between the high and low temperature applied field vs. magnetization curves along with the decreasing gap between the field cooled and zero field cooled curves in Figure 34, show that the film may be near its T_C.

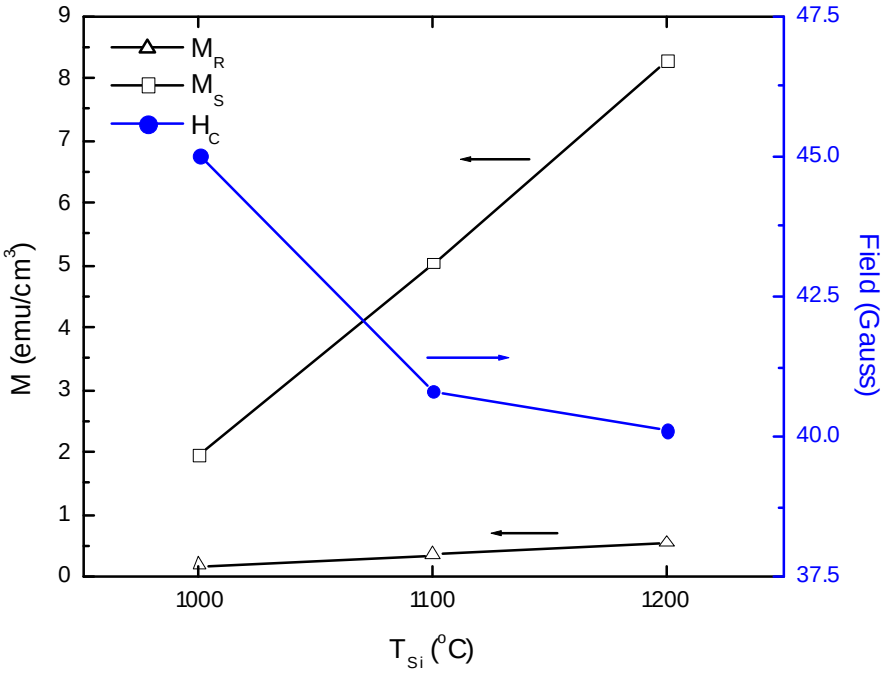

Figure 33. Saturation Magnetization, coercivity, and remnant magnetization vs. silicon cell temperature. Saturation magnetization taken at 1000 Gauss from magnetization vs. applied field curves taken at 300K. Coercivity and remnant magnetization also read from magnetization vs applied field measurements at 300K.

In conclusion, GaN:Gd films have been grown which are ferromagnetic above room temperature and reject interfacial effects as the root of this behavior. The incorporation of Gd into the films is extremely low and results in highly resistive films. The ferromagnetic behavior of this material follows models of long range spin polarization. In addition, co-doping with Si shows larger overall magnetic signal and results in a conductive, n-type material. Further work should be performed to attain p-type material.

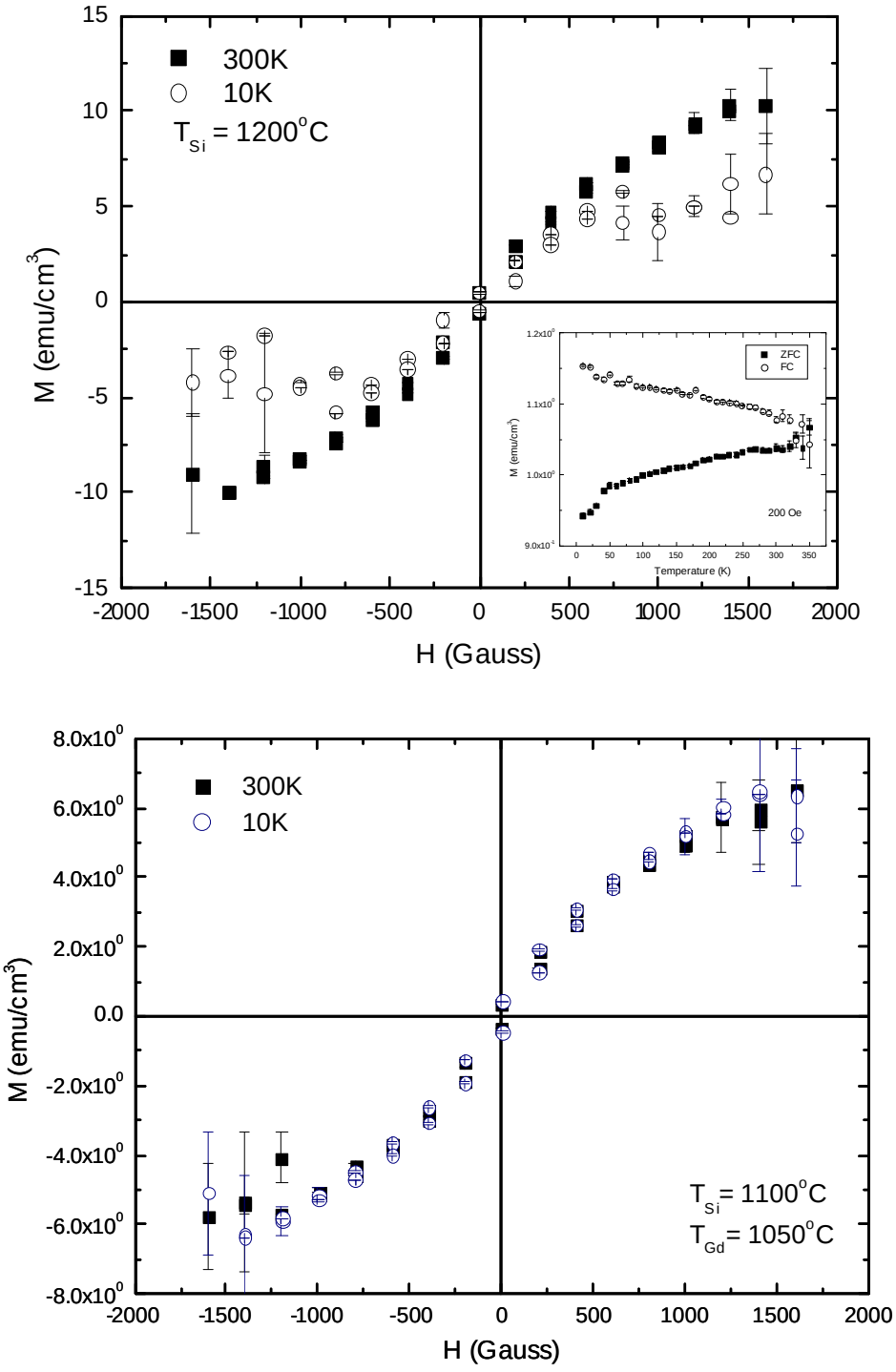

Figure 34. Magnetization curves for GaN:Gd,Si grown at T_{Si} = 1200ºC at top, and T_{Si} = 1100ºC at bottom. Magnetization vs. applied field at 10 K and 300 K shown as large image, inset contains. Magnetization vs. temperature at an applied field of 200 Oe, showing both field cooled and zero field cooled traces at bottom.

The thermal stability of the optimal GaN:Gd (T_{Gd} = 1050°C) was investigated in a systematic way. The GaN:Gd was annealed from 300°C to 700°C to determine the temperature at which magnetization is destroyed. M vs. H measurements taken at 300K for each anneal temperature indicate the change in magnetization with anneal temperature. Figure 35 shows the saturation magnetization vs. the anneal temperature (T_{anneal}). After the first anneal at 300°C the saturation magnetization immediately decreases from the as grown value and generally decreases as the anneal temperature increases. This is a possible indication of the destruction of the magnetic properties of the film. However, the M vs. H depicts a different scenario. Figure 36 compares the M vs. H of the as grown GaN:Gd to that annealed at 600°C. As shown in figure 35, the saturation magnetization decreases by a factor of greater than one half. Although the maximum magnetic signal decreases, the overall hysteresis increases. The loop becomes more square, with an increase in magnetic remanence and coercivity. This broadening of the remanence and coercivity indicates a "hardening" of the ferromagnetism. One possible explanation of the hardening involves a change in domain structure. The high anneal temperature may alter the domain structure in such a way as to make the domains less easy to manipulate, thereby requiring a stronger magnetic field to produce zero magnetization. The increase in remanence with anneal temperature indicates the retention of more magnetic alignment within the material. Therefore, it seems plausible that annealing the GaN:Gd creates an alteration within the domain structure producing a larger coercivity and remanence. Also, the decrease in saturation magnetization indicates a decrease in the strength of the magnetic interactions within the GaN:Gd, however the magnetization remains even after a 700°C anneal. This retention of magnetization after a high temperature anneal is an improvement in thermal stability compared to the Cr-doped AlN.

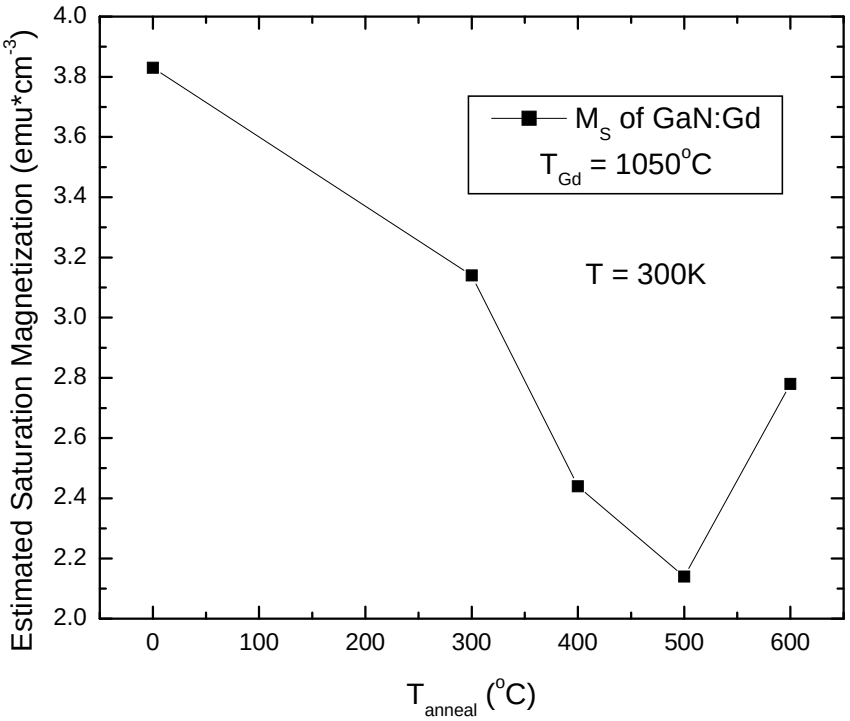

Figure 35. Estimated saturation magnetization vs. anneal temperature for GaN:Gd with T_{Gd} = 1050°C.

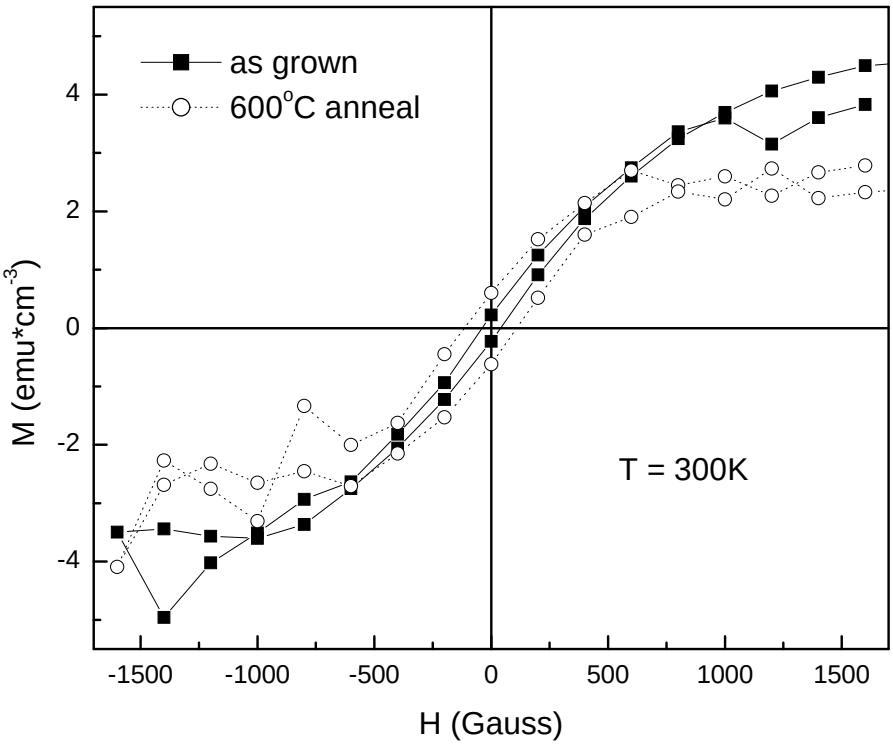

Figure 36. Magnetization vs. applied field comparing the as grown GaN:Gd to that annealed at 600°C.

The M vs. T corroborates the existence of magnetism after the 700°C anneal. Figure 37 shows the separation in the field-cooled and zero field-cooled loops up to about 320K. Above 320K, the M vs. T suggests the magnetization is reduced greatly. This is also seen in the M vs. H at 350K as compared to 50K, shown in Figure 7.38. The overall hysteresis is decreased at 350K, with a lower coercivity and field at which the material saturates. Although the hysteresis is beginning to vanish at 350K, the GaN:Gd annealed at 700°C remains ferromagnetic at 300K, as shown in Figure 39. This result was not found for the material doped with transition metals, as discussed in Chapter 5. This suggests that the magnetic interaction within the GaN:Gd is not destroyed after a high temperature anneal. Moreover, it implies that Gd is a superior dopant to the transition metals.

The incorporation of Gd into GaN results in an overall improvement of magnetic properties. The magnetization is increased although the dopant concentration is lower. More importantly, the ferromagnetism persists even after a 700°C anneal. This results in the possibility of incorporating GaN:Gd into spintronic devices which require a high temperature anneal without destroying the magnetic properties. The application of GaN:Gd into spintronic devices will rely on other material characteristics such as transport, which will require investigation. Also, the impact of Gd on conductivity requires further investigation. One possible method is to use current-voltage measurements to probe the impurity within a quantum well. This should show whether the impurity is a distribution of levels or a single level. Although more investigation is needed to probe the effectiveness of GaN:Gd, the initial findings suggest it is superior to other III-N DMS.

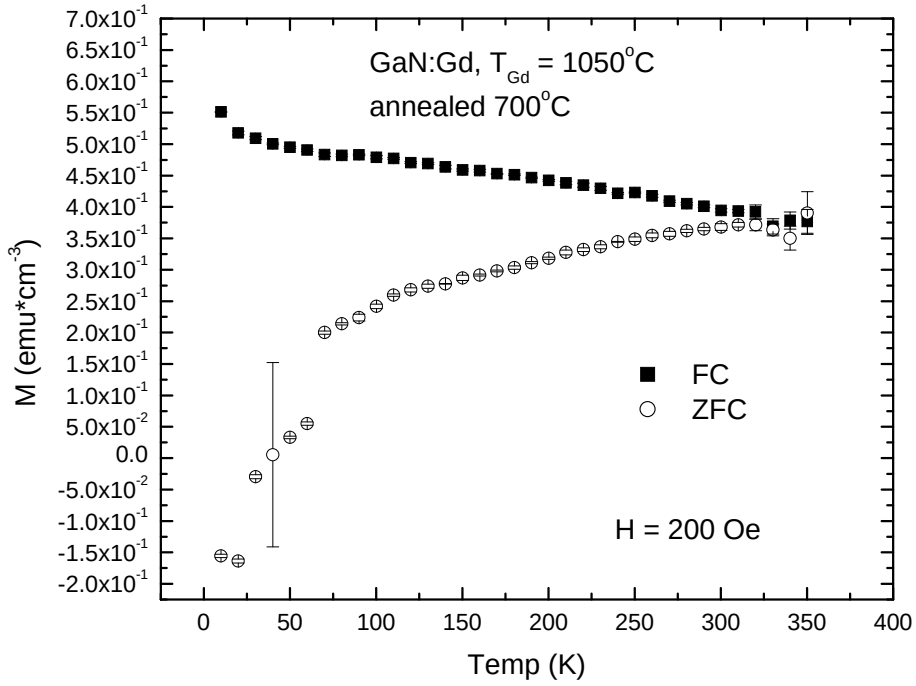

Figure 37. Magnetization vs. temperature of GaN:Gd after 700°C anneal.

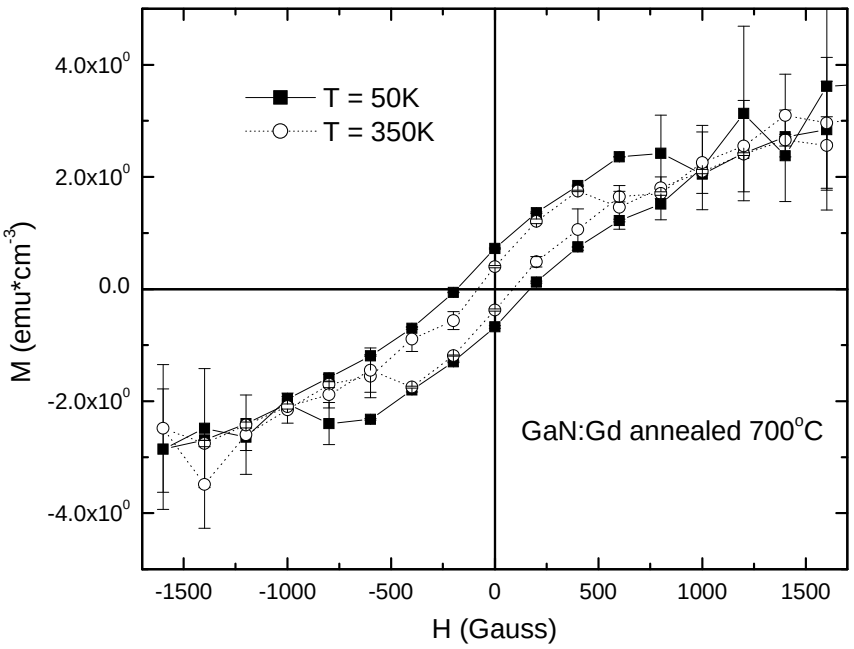

Figure 38. Magnetization vs. applied field at 50K and 350K for GaN:Gd annealed at 700°C.

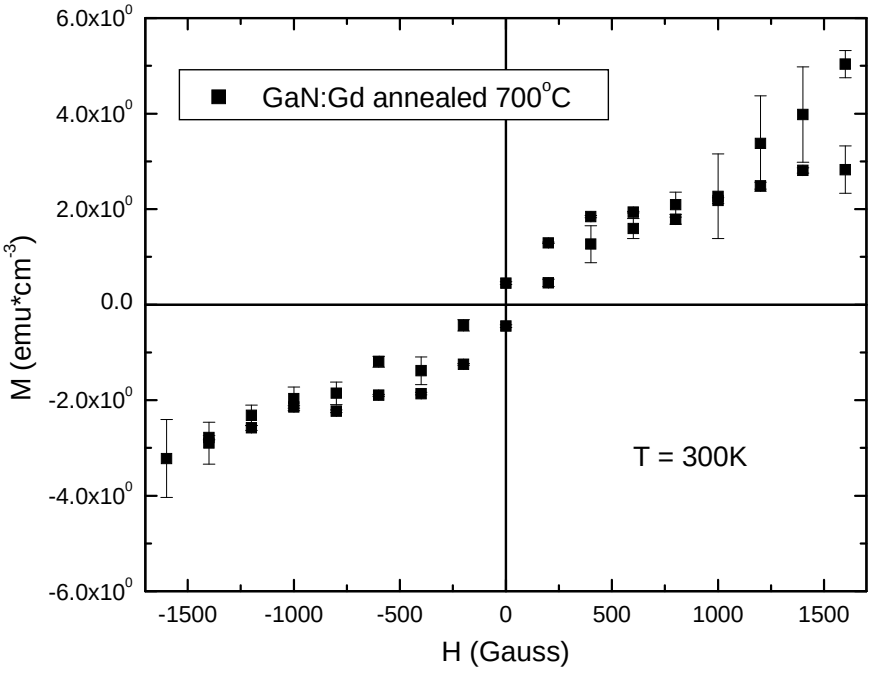

Figure 39. Magnetization vs. applied field at 300K for GaN:Gd annealed at 700°C.

2.5 OPTICAL AND MAGNETIC PROPERTIES OF EU-DOPED GALLIUM NITRIDE

Eu-doped samples were grown by MBE on *c*-plane sapphire substrates. A low temperature, 50nm thick AlN buffer was followed by growth of ~0.5μm of GaN:Eu at 800°C with a Eu cell temperature of 470°C. The Ga flux during growth was varied from 3.0×10^{-7} to 5.4×10^{-7} Torr by controlling the Ga cell temperature in the range of 860–890°C. The samples were capped with an additional 50 nm of low temperature AlN and annealed at 675°C for 100min. This produces a Eu concentration in the range of 0.12at.%, as determined by Rutherford backscattering. [28] This is a much lower concentration than used in previous work (2at.%).[22] Previous measurements have also shown the presence of a significant concentration of oxygen in the samples, which tends to increase the population of the +3 valence state.[9] The samples were insulating and were characterized by room temperature photoluminescence (PL) measurements using a HeCd laser (325nm) as an excitation source and also by x-ray diffraction (XRD) measurements in a powder system. We also performed some preliminary θ-2θ measurements using a double-crystal system. Magnetic measurements were taken up to room temperature (300K) with a Quantum Design magnetic properties measurement system superconducting quantum interference device magnetometer. The magnetic field was applied vertical to the sample surface in all cases, the easy axis of magnetization.[22] The diamagnetic properties of the substrate and holder were subtracted out and the data normalized to sample volume.

The PL spectra from the GaN:Eu samples are shown in Fig. 40 as a function of the Ga flux during growth. The spectra show a strong dominant emission at 622nm due to the intra-atomic transitions inside the 4*f* shell of Eu^{3+} ions ($^5D_0$-$^7F_2$ transition).[22] The less dominant transition around 599 nm is attributed to Eu^{3+} 4*f* inner shell transitions from $^5D_0$ to $^7F_1$. [15] This is

consistent with previous reports that show a correlation between the 622nm emission and a majority of the Eu ions being in the 3+ state in the GaN, [22,29] with the Eu occupying substitutional Ga sites as determined by extended x-ray absorption fine structure measurements.[29] Note that the PL emission intensity is a maximum at lower Ga fluxes, consistent with the Eu occupying Ga sites. While the III-nitrides have proven quite successful for fabrication of blue and green light emitting devices, realization of red devices has been less successful due to the difficulties associated with the synthesis of the high-In-content InGaN needed to achieve red emission. An attractive alternative may be the use of Eu-doped GaN, whose emission wavelength is host-material insensitive. GaN is an attractive host for optical centers as its wide band gap has been shown to reduce thermal quenching in Er^{+3}-doped material. This reduction in quenching allows efficient operation of Er-doped material at room temperature [15,16,17,18] and should offer the same benefit for Eu^{3+}.

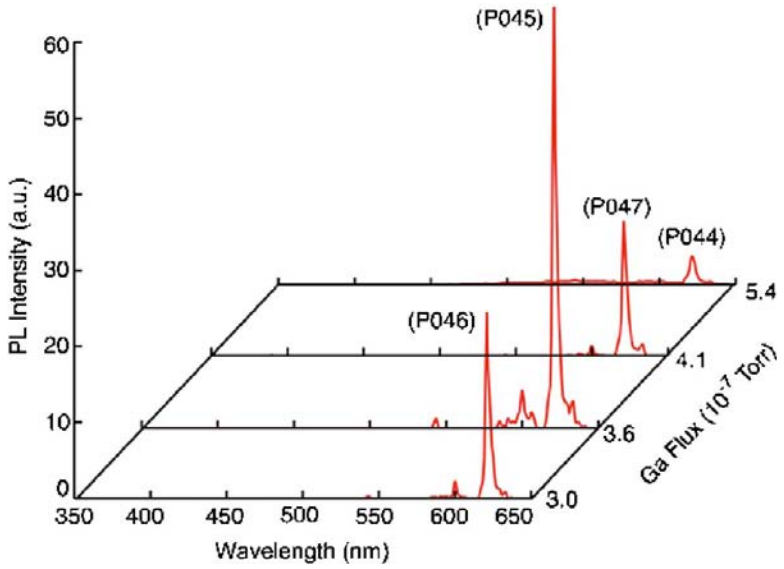

Figure 40 PL spectra at 300 K from Eu-doped GaN samples grown with different Ga fluxes

Figure 41 shows the magnetization (*M*) versus field (*H*) behavior at 300K for the Eu-doped sample grown with the lowest Ga flux (3×10^{-7}Torr). Hysteretic behavior is clearly observed, consistent with ferromagnetism. Other possible explanations for hysteretic *M* vs *H* behavior that are remotely possible include super-paramagnetism and spin-glass effects. These films also appear to have Curie temperatures (T_C) around room temperature, as shown from the lack of closure between the field-cooled and zero-field-cooled lines in the magnetization vs temperature curves at the bottom of Fig. 41. Magnetization measurements were also performed on undoped GaN samples to eliminate the possibility that spurious transition metal impurities might be responsible for the magnetic response. These exhibited no magnetic hysteresis, showing that the Eu doping is responsible for the observed magnetization.

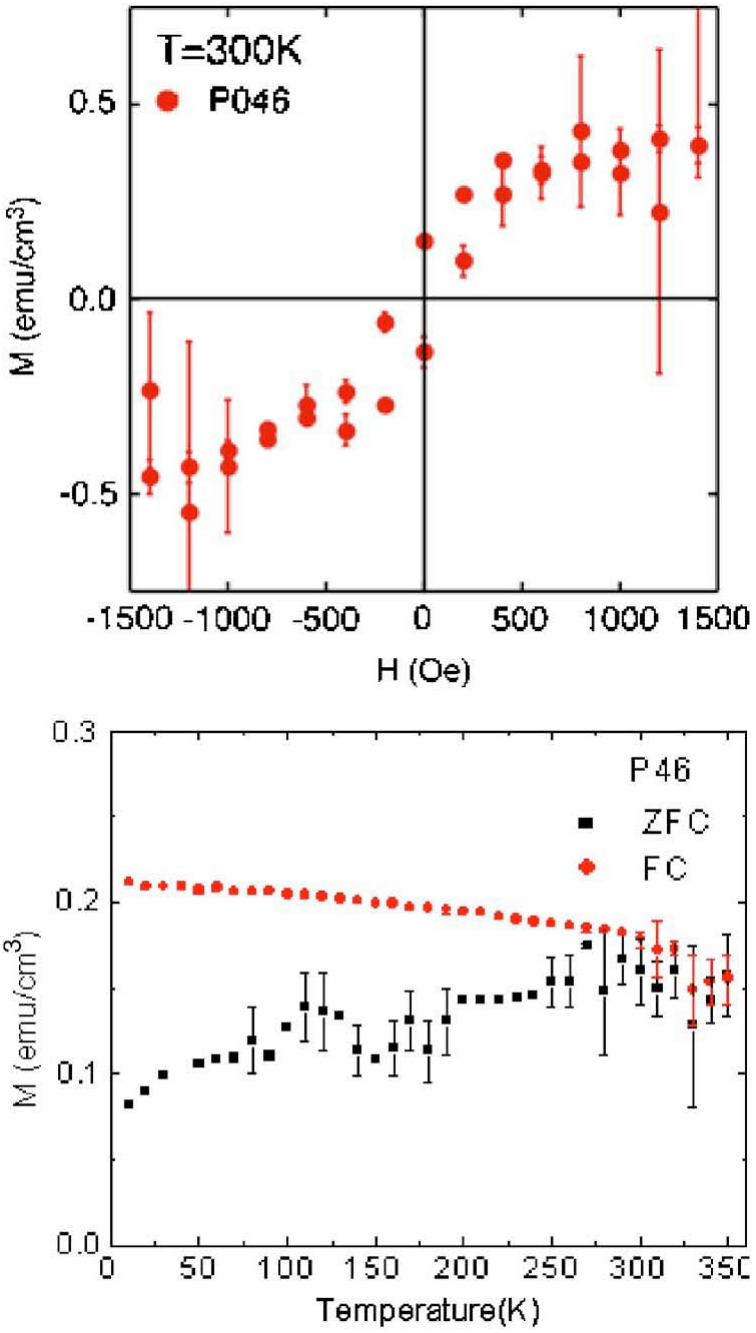

Figure 41 300K magnetization vs field curve from Eu-doped GaN grown with a Ga flux of 3.6×10^{-7} Torr (top) and field-cooled and zero-field-cooled magnetizations as a function of temperature (bottom).

Figure 42 shows the saturation magnetization and PL intensity at 300K as a function of the Ga flux during growth of the GaN:Eu. There is an inverse correlation between the two parameters and the 300 and 10K magnetizations roughly track each other. The PL intensity is a maximum at moderate Ga fluxes, as discussed above. Previous reports have suggested that the ferromagnetism

in Eu-doped GaN is due to Eu^{2+} ions because of their large total angular momentum in the ground state, while the Eu^{3+} would lead to paramagnetism. [22] In this scenario, the higher population of the trivalent states at moderate Ga fluxes would correlate with a lower saturation magnetization, as observed. The minima/maxima in Fig.42 might be explained as follows. The +2/+3 ratio decreases with increasing Ga flux. However, as the Ga flux increases (we are always in N-rich growth conditions), the Eu gets increasingly tied up as Eu–Ga phases, leaving less substitutional Eu. The Eu that remains prefers to be increasingly +3, enhancing the optical activity over the magnetic activity. The Eu–Ga phases are only weak antiferromagnets, and would be well into paramagnetism for the Fig. 42 measurements at 300 K, and not contributing to any remaining ferromagnetism. A spatial variation in Eu^{3+}/Eu^{2+} concentration ratio in GaN has previously been noted from resonant photoemission measurements. [30] The saturation magnetization in our films is comparable to previous reports even though the Eu concentration is approximately a factor of 16 lower. [22]

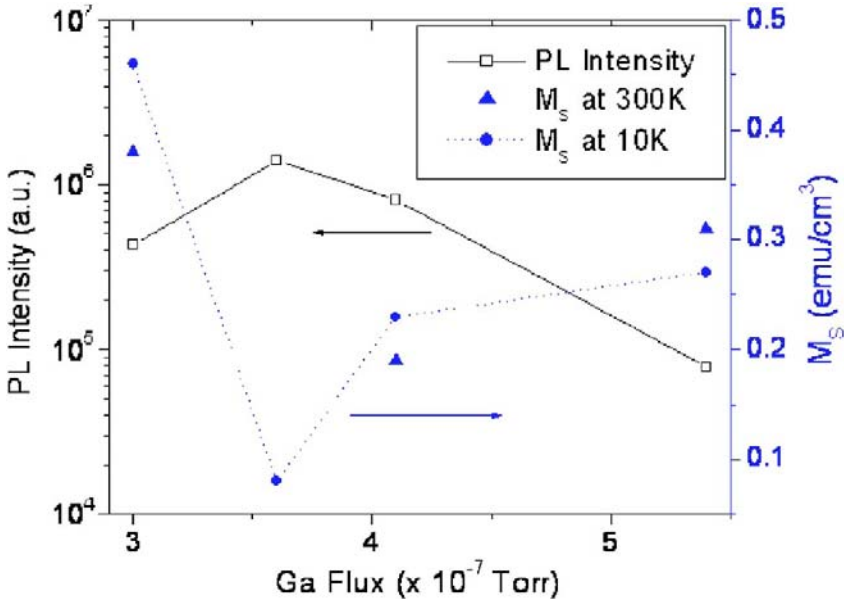

Figure 42 PL intensity at 300K and saturation magnetization at a field of 1500Oe at both 10 and 300K from Eu-doped GaN as a function of Ga flux during growth.

Figure 43 shows the XRD spectrum from Eu-doped GaN grown with the lowest Ga flux. We observe the presence of a Eu–Ga phase in addition to the usual GaN peaks. Similar results were obtained for all of our samples. In analogy with the case of Gd in GaN (Ref. 31) and the heat of formation of the respective compounds, [32,33] it might be expected that the reaction $Eu+GaN \rightarrow Ga+EuN+Ga_xEu_yN$ may occur and that the Eu can then form alloys of Eu_xGa_y. Our double-crystal measurements show that at least two different EuGa phases (EuGa and $EuGa_2$) are present. There may be others present below the concentration limit of our system, but none of the Eu–Ga phases are ferromagnetic at high temperatures. Indeed, the respective Néel temperatures are 18K (EuGa), 22K ($EuGa_2$), 10–15K ($EuGa_4$), 23K (Eu_3Ga_8), and 33K (Eu_5Ga_8).[34,35] Bulk Eu has a Néel temperature of 90K, while there are no EuN phases with high Curie temperatures

(at 77K EuN is paramagnetic). [36] In addition, the magnetic semiconductor EuO has a Curie temperature of ~77K, [32] so it does not appear to be a factor in the observed magnetic properties, while Eu_3O_4 has a Curie temperature of 7.8K and Eu_2O_3 is paramagnetic. [37]

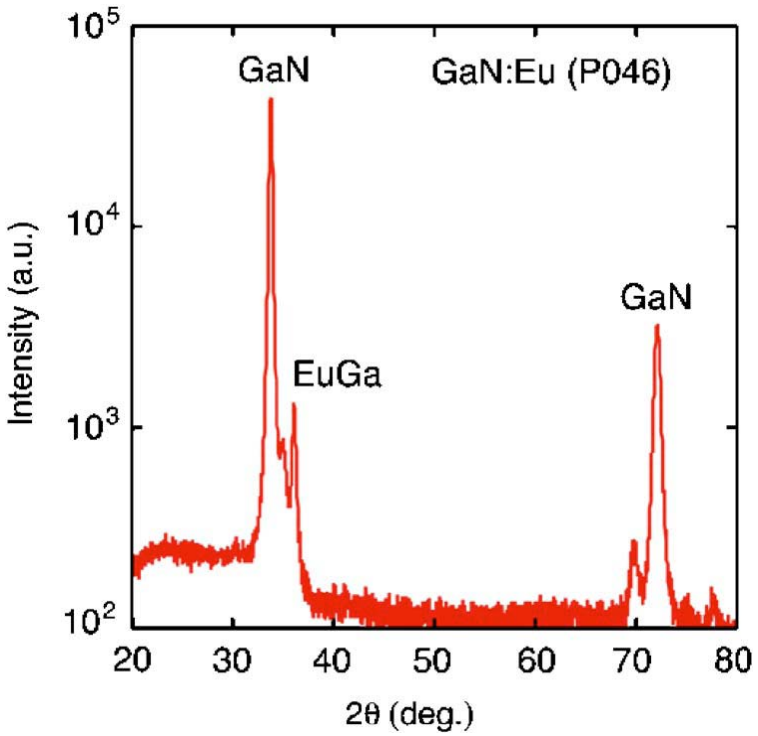

Figure 43 XRD spectrum from Eu-doped GaN grown with a Ga flux of 3.6×10^{-7} Torr.

In conclusion, Eu-doped GaN shows both strong red emission at 622nm from the $^5D_0 \rightarrow {}^7F_2$ transition of Eu^{+3} and hysteretic behavior in the field dependence of magnetization, consistent with the presence of a ferromagnetic phase. This material appears very promising for multifunctional devices with both optoelectronic and magnetic functions.

3.0 REFERENCES

1. H. Ennen, J. Schneider, G. Pomrenke, and A. Axmann, Appl. Phys. Lett. **43**, 943 (1983).
2. J. M. Zavada and D. Zhang, Solid-State Electron. **38**, 1285 (1995).
3. R. G. Wilson, R. Schwartz, C. R. Abernathy, S. J. Pearton, N. Newman, M. Rubin, T. Fu, and J. M. Zavada, Appl. Phys. Lett. **65**, 992 (1994).
4. X. Wu, U. Hommerich, J. D. MacKenzie, C. R. Abernathy, S. J. Pearton, R. Schwartz, R. G. Wilson, and J. M. Zavada, Appl. Phys. Lett. **70**, 2126 (1997).
5. X. Wu, U. Hommerich, J. D. MacKenzie, C. R. Abernathy, S. J. Pearton, R. G. Wilson, R. N. Schwartz, and J. M. Zavada, J. Lumin. **72–74**, 284 (1997).

6. S. J. Pearton, C. R. Abernathy, J. D. MacKenzie, R. G. Wilson, R. N. Schwartz, and J. M. Zavada, Appl. Phys. Lett. **71**, 1807 (1997).

7. A. Steckl and R. Birkhahn, Appl. Phys. Lett. **73**, 1700 (1998).

8. E. Alves, M. F. da Silva, J. C. Soares, J. Bartels, R. Vianden, C. R. Abernathy, and S. J. Pearton, MRS Internet J. Nitride Semicond. Res. **451**, G11-2 (1999).

9. A. J. Steckl and J. M. Zavada, MRS Bull. **24**, 33 (1999).

10. R. Birkhahn, M. Garter, and A. J. Steckl, Appl. Phys. Lett. **74**, 2161 (1999).

11. K. Gurumurugan, M. Chen, G. Harp, W. Jadwisienczak, and H. Lozykowski, Appl. Phys. Lett. **74**, 3008 (1999).

12. W. Jadwisienczak, H. Lozykowski, I. Berishev, A. Bensaoula, and I. Brown, J. Appl. Phys. **89**, 4384 (2001).

13. H. J. Lozykowski, W. M. Jadwisienczak, and I. Brown, Appl. Phys. Lett. **74**, 1129 (1999).

14. A. J. Steckl, M. Garter, D. S. Lee, J. Heikenfeld, and R. Birkhahn, Appl. Phys. Lett. **75**, 2184 (1999).

15. D. S. Lee, J. Heikenfeld, R. Birkhahn, M. Garter, B. K. Lee, and A. J. Steckl, Appl. Phys. Lett. **76**, 1525 (2000).

16. J. Heikenfeld, M. Garter, D. S. Lee, R. Birkhahn, and A. J. Steckl, Appl. Phys. Lett. **75**, 1189 (1999).

17. S. Morishima, T. Maruyama, M. Tanaka, Y. Masumoto, and K. Akimoto, Phys. Status Solidi A **176**, 113 (1999).

18. M. E. Overberg, K. N. Lee, C. R. Abernathy, S. J. Pearton, W. S. Hobson, R. G. Wilson, and J. M. Zavada, Mater. Sci. Eng., B **81**, 150 (2001).

19. A. J. Steckl, J. C. Heikenfeld, D. S. Lee, M. J. Garter, C. C. Baker, Y. Wang, and R. Jones, IEEE J. Sel. Top. Quantum Electron. **8**, 749 (2002).

20. K. Lorenz, U. Wahl, E. Alves, S. Dalmasso, R. W. Martin, K. P. O'Donnell, S. Ruffenach, and O. Briot, Appl. Phys. Lett. **85**, 2712 (2004).

21. N. Teraguchi, A. Suzuki, Y. Nanishi, Y.-K. Zhou, M. Hashimoto, and H. Asahi, Solid State Commun. **122**, 651 (2002).

22. M. Hashimoto, A. Yanase, R. Asano, H. Tanaka, H. Bang, K. Akimoto, and H. Asahi, Jpn. J. Appl. Phys., Part 2 **42**, L1112 (2003).

23. S. Dhar, O. Brandt, M. Ramsteiner, V. F. Sapega, and K. H. Ploog, Phys. Rev. Lett. **94**, 037205 (2005).

24. S. Dhar, L. Perez, O. Brandt, A. Trampert, K. H. Ploog, J. Keller, and B. Beschoten, Phys. Rev. B **72**, 245203 (2005).

25. S. Y. Han, J. Hite, G. T. Thaler, R. M. Frazier, C. R. Abernathy, S. J. Pearton, H. K. Choi, W. O. Lee, Y. D. Park, J. M. Zavada, and R. Gwilliam, Appl. Phys. Lett. **88**, 042102 (2006).

26. H. Asashi, Y. K. Zhou, M. Hashimoto, M. S. Kim, X. J. Lin, S. Emura, and S. Hasegawa, J. Phys.: Condens. Matter **16**, S5555 (2004).

27. G. M. Dalpian and S.-H. Wei, Phys. Rev. B **72**, 115201 (2005).

28. K. Lorenz, R. Vianden, R. Birkhahn, A. J. Steckl, M. F. da Silva, J. C. Soares, and E. Alves, Nucl. Instrum. Methods Phys. Res. B **161/163**, 950 (2000).

29. H. Bang, S. Morishima, Z. Li, K. Akimoto, M. Nomura, and E. Yagi, J. Appl. Phys. **237–239**, 1027 (2002).

30. T. Maruyama, S. Morishima, H. Bang, K. Akimoto, and Y. Nanishi, J. Cryst. Growth **237–239**, 1167 (2002).

31. W. Xiao, Q. Guo, Q. Xue, and E. G. Wang, J. Appl. Phys. **94**, 4847 (2003).

32. *Handbook on the Physics and Chemistry of Rare Earths*, edited by K. A. Gschneider, Jr. and L. R. Eyling (North-Holland, Amsterdam, 1979), Vol. 2, 76.

33. *Binary Alloy Phase Diagrams*, edited by T. B. Massalski (ASM International, Metals Park, OH, 1992), 217.

34. J. DeVries, R. Thiel, and K. Buschow, Physica B **128**, 265 (1985).

35. S. Bobev, E. D. Bauer, J. D. Thompson, and J. L. Sarrao, J. Magn. Magn. Mater. **277** 236 (2004).

36. R. Didchenko and F. P. Gortsema, J. Phys. Chem. Solids **24**, 863 (1963).

37. *The Oxide Handbook*, edited by G. V. Samsonov (IFI/Plenum, New York, 1973), 402 (translated from Russian by C. Nigel Turton and Tatiana I. Turton).

4.0 JOURNAL PUBLICATIONS

1. "Effect of Oxygen Co-Doping on the Electronic and Magnetic Properties of GaMnN," G. Thaler, R. Frazier, B. Gila, J. Stapleton, R. Davies, C.R. Abernathy and S.J. Pearton, Electrochem. Solid-State Lett. 8 G20 (2005).
2. "Electrical and Optical Properties of GaCrN Films Grown by Molecular Beam Epitaxy," A.Y. Polyakov, N. Smirnov, A. Govorkov, G.T. Thaler, R. Frazier, C.R. Abernathy and S.J. Pearton, J. Vac. Sci. Technol. B 23 1 (2005).
3. "Role of Growth Conditions on Magnetic Properties of AlCrN Grown by Molecular

Beam Epitaxy," R. Frazier, G.T. Thaler, J.Y. Leifer, J.K. Hite, B.P. Gila, C.R. Abernathy and S.J. Pearton, Appl. Phys. Lett. 86 052101 (2005).

4. "Growth and Thermal Stability of Ga(1–X)CrXN Films," G.T. Thaler, R.M. Frazier, C.R. Abernathy and S.J. Pearton, Appl. Phys. Lett. 86 131901 (2005).
5. "AlN-based Dilute Magnetic Semiconductors," R.M. Frazier, G.T. Thaler, B.P. Gila, J. Stapleton, M.E. Overberg, C.R. Abernathy, S.J. Pearton, F. Ren and J.M. Zavada, J. Electron. Mater. 34 365 (2005).
6. "Efficient spin relaxation in InGaN/GaN and InGaN/GaMnN quantum wells: An obstacle to spin detection, W. M. Chen et al., Appl. Phys. Lett. 87, 192107 (2005)
7. "Ultraviolet photoluminescence from Gd-implanted AlN epilayers," Appl. Phys. Lett. 89, 152107 (2006), J. M. Zavada, N. Nepal, J. Y. Lin, H. X. Jiang, U. Hömmerich, J. Hite, G. T. Thaler, C. R. Abernathy, and S. J. Pearton
8. "Optical and magnetic properties of Eu-doped GaN," Appl. Phys. Lett. 89, 132119 (2006); J. Hite, G. T. Thaler, R. Khanna, C. R. Abernathy, S. J. Pearton, J. H. Park and A. J. Steckl, J. M. Zavada
9. "Effect of growth conditions on the magnetic characteristics of GaGdN," J. K. Hite, R. M. Frazier, R. Davies, G. T. Thaler, C. R. Abernathy, S. J. Pearton, and J. M. Zavada Appl. Phys. Lett. 89, 092119 (2006)
10. "Effect of Gd implantation on the structural and magnetic properties of GaN and AlN," Appl. Phys. Lett. 88, 042102 (2006), Sang Youn Han, J. Hite, G. T. Thaler, R. M. Frazier, C. R. Abernathy, and S. J. Pearton, W. O. Lee, and Y. D. Park, J. M. Zavada
11. "Effect of SiCo doping on ferromagnetic properties of GaGdN," Hite, JK; Frazier, RM; Davies, RP; Thaler, G. T; Abernathy, CR; Pearton, SJ; Zavada, JM; Brown, E; Hommerich, U, Journal Of Electronic Materials, 36, 391(2007).
12. "Magneto-optical spectroscopy of spin injection and spin relaxation in ZnMnSe/ZnCdSe and GaMnN/InGaN spin light-emitting structures," Buyanova, IA; Chen, WM; Oka, Y; Abernathy, CR; Pearton, SJ Buyanova, I. A.; Chen, W. M.; Oka, Y.; Abernathy, C. R.; Pearton, S. J., Physica Status Solidi A-Applications And Materials Science, 0031-8965, JAN (2007) 204.

5.0 PRESENTATIONS

Invited

"Development of Gallium Nitride based dilute magnetic semiconductors for magneto-optical applications," Florida AVS Meeting, March 2005, G. T. Thaler

"Ferromagnetism in Transition Metal Doped GaN and Related Materials", APS Meeting, March, 2005, C. R. Abernathy

6.0 Students Supported

1) Rachel Frazier, Ph.D. graduated 8/2005
2) Jennifer Hite, Ph.D. graduated 12/2006
3) Ryan Davies, Ph.D. expected graduation date 2009